

1 **High throughput PRIME editing screens identify functional DNA variants in the human
2 genome**

3

4 **Authors:** Xingjie Ren^{1,*}, Han Yang^{1,*}, Jovia L. Nierenberg², Yifan Sun¹, Jiawen Chen³, Cooper
5 Beaman¹, Thu Pham⁴, Mai Nobuhara⁴, Maya Asami Takagi¹, Vivek Narayan¹, Yun Li^{3,5,6}, Elad
6 Ziv^{1,7}, Yin Shen^{1,8,9,#}

7

8 **Affiliations**

9 ¹ Institute for Human Genetics, University of California, San Francisco, San Francisco, CA, USA.

10 ² Department of Epidemiology and Biostatistics, University of California, San Francisco, San
11 Francisco, CA, USA.

12 ³ Department of Biostatistics, University of North Carolina at Chapel Hill, Chapel Hill, NC 27599,
13 USA.

14 ⁴ Pharmaceutical Sciences and Pharmacogenomics Graduate Program, University of California,
15 San Francisco, San Francisco, CA, USA.

16 ⁵ Department of Genetics, University of North Carolina, Chapel Hill, NC, USA.

17 ⁶ Department of Computer Science, University of North Carolina, Chapel Hill, NC, USA.

18 ⁷ Division of General Internal Medicine, Department of Medicine, and Helen Diller Family
19 Comprehensive Cancer Center, University of California, San Francisco, San Francisco, CA, USA.

20 ⁸ Department of Neurology, University of California, San Francisco, San Francisco, CA, USA.

21 ⁹ Weill Institute for Neurosciences, University of California, San Francisco, San Francisco, CA,
22 USA.

23 * These authors contributed equally to the work.

24 #Corresponding authors: Yin Shen Yin.Shen@ucsf.edu

25 **Abstract**

26 Despite tremendous progress in detecting DNA variants associated with human disease,
27 interpreting their functional impact in a high-throughput and base-pair resolution manner remains
28 challenging. Here, we develop a novel pooled prime editing screen method, PRIME, which can
29 be applied to characterize thousands of coding and non-coding variants in a single experiment
30 with high reproducibility. To showcase its applications, we first identified essential nucleotides for
31 a 716 bp *MYC* enhancer via PRIME-mediated saturation mutagenesis. Next, we applied PRIME
32 to functionally characterize 1,304 non-coding variants associated with breast cancer and 3,699
33 variants from ClinVar. We discovered that 103 non-coding variants and 156 variants of uncertain
34 significance are functional via affecting cell fitness. Collectively, we demonstrate PRIME capable
35 of characterizing genetic variants at base-pair resolution and scale, advancing accurate genome
36 annotation for disease risk prediction, diagnosis, and therapeutic target identification.

37 **Main**

38 Advances in genome sequencing have led to the identification of hundreds of millions of
39 genetic variants in the human population, with a fraction conferring risk for common illnesses such
40 as diabetes, neurological disorders, and cancers¹. A major barrier to understanding the genetic
41 underpinnings of these complex diseases is the paucity of functional annotation for disease-
42 associated variants, especially because such variants are predominantly located within non-
43 coding regions. Growing evidence suggests that non-coding risk variants may contribute to
44 disease pathogenesis by disrupting gene regulation. Even protein-coding variants discovered
45 from individuals with disease are frequently classified as Variants of Uncertain Significance
46 (VUS). Therefore, more precise and higher throughput functional characterization methods for
47 elucidating disease-associated variant function at base-pair resolution, and multiplexed across
48 genomic loci, are necessary to realize the potential of personalized medicine.

49 The development of genome editing technologies has enabled us to perturb and assess
50 DNA sequences in desired regions at a large scale. However, there are still fundamental barriers
51 to utilizing these methods for precision genome annotation. For example, CRISPRa, CRISPRi,
52 CRISPR deletion, and CRISPR indel have been applied in genetic screening strategies for
53 characterizing both genes and *cis*-regulatory regions², but have failed to pinpoint causal variants
54 for diseases. Traditional methods of characterizing DNA variants (SNPs) by knock-in via
55 homologous recombination are inefficient and low throughput. Base editors also have limitations,
56 introducing specific mutations (C→T, A→G, T→C, G→A) with varied target efficiencies³. Thus,
57 there is still a significant deficit in methods for effectively characterizing the roles of putative
58 disease-causing variants in human health and diseases. Robust high throughput methods making
59 desired edits at base-pair resolution are urgently needed to achieve a better understanding of the
60 genetic underpinnings of disease.

61 Prime editing (PE), a versatile and precise genetic engineering method, has been
62 developed to introduce any type of edit, including point mutation, insertion, and deletion⁴. In
63 particular, PE2, employs the *Streptococcus pyogenes* Cas9 (SpCas9) H840A nickase and
64 Moloney murine leukemia virus (M-MLV) reverse transcriptase. The spacer in the prime editing
65 guide RNA (pegRNA) directs the Cas9 nickase and M-MLV complex to the target site, while the
66 RT template sequence provides the desired editing information. Thus, both targeting and editing
67 information can be easily programmed in the same pegRNA to perform single nucleotide
68 substitution, insertion or deletion. PE3, a newer iteration of PE, can further increase editing
69 efficiency by promoting the replacement of non-edited strands using an additional single-guide
70 (sgRNA) for nicking⁵. Prime editors' capacity for precision genome editing suggests the possibility

71 of high throughput variant-level genome manipulation. Recently, PE screens were used to identify
72 VUS at the *NPC1* locus based on a lysosome functional assay by transfection of pegRNAs and
73 targeted sequencing of this region⁶. Although transient transfection of PE machinery followed by
74 targeted sequencing of the edited locus enables the identification of editing events, its scope is
75 limited to just that locus, and thus, scaling up for massively parallel assessment of multiple loci is
76 not feasible. Besides increased throughput, improved control of transgene copy number, stable
77 expression of PE machinery, and direct loci comparison are also desired.

78 Here, we enable high throughput pooled screens of thousands of DNA variants in the
79 human genome by lentiviral delivery of PE, namely PRIME. We demonstrate the utility of PRIME
80 for three different applications, including the saturation mutagenesis analysis of a 716 bp
81 enhancer, the functional characterization of 1,304 breast cancer-associated variants, and the
82 evaluation of 3,699 clinical variants' impact on cell fitness. Our results establish the
83 generalizability of PRIME for precisely characterizing genetic variants in the human genome.

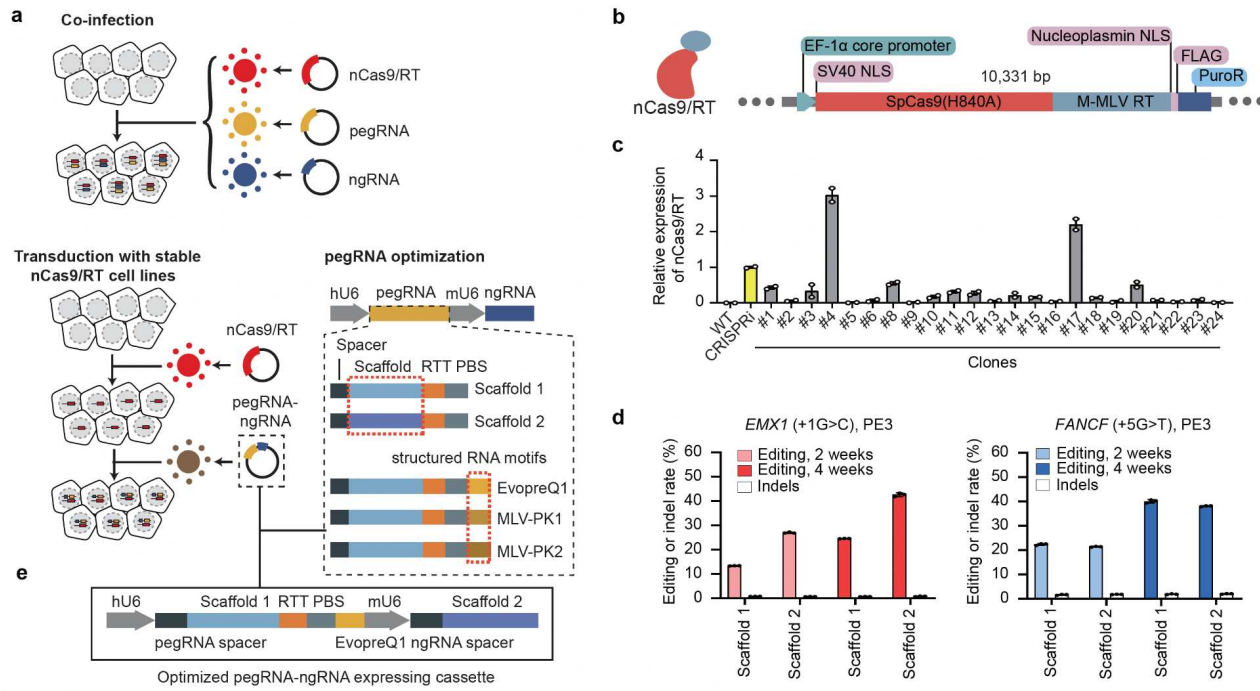
84

85 **Optimization of PE efficiency in mammalian cells delivered by lentivirus**

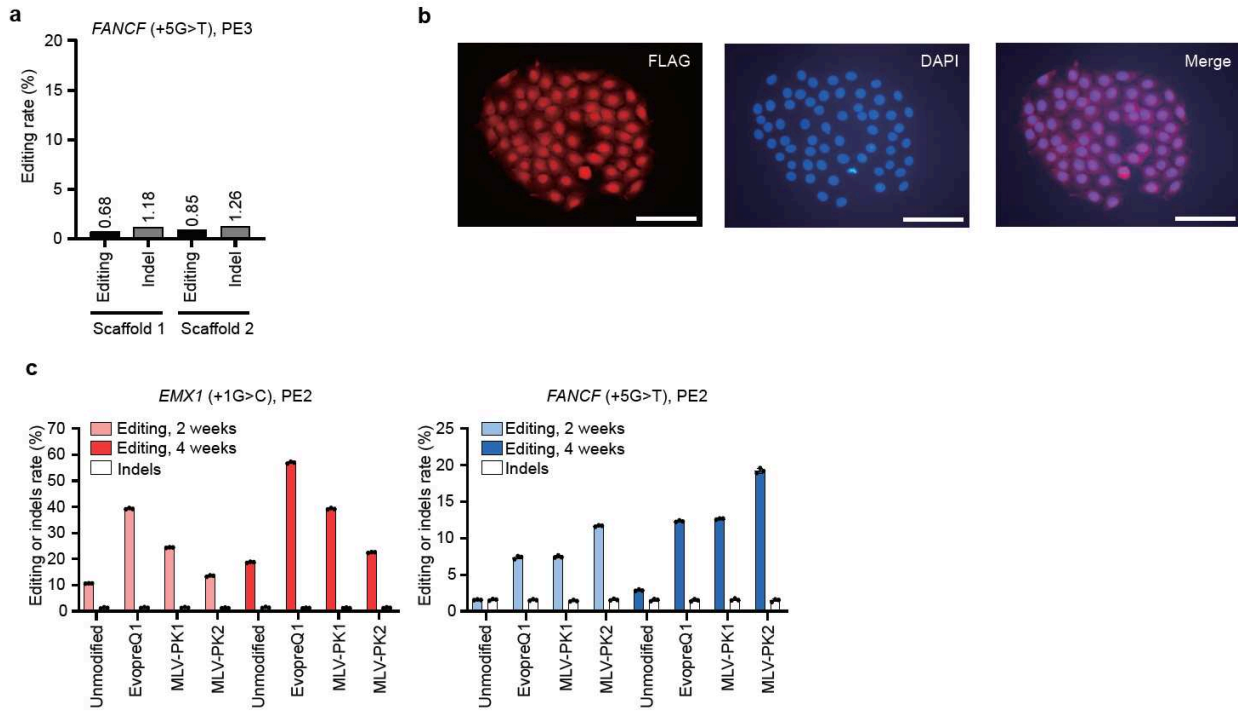
86 To enable PE screens with delivery by lentivirus, we initially installed PE3 by infecting
87 MCF7 cells using three different viruses: 1) virus expressing Cas9 (H840A) nickase (nCas9) and
88 Moloney murine leukemia virus (M-MLV) reverse transcriptase; 2) virus expressing pegRNA; 3)
89 virus expressing nick sgRNA (ngRNA). Unfortunately, this strategy yielded less than 1% PE
90 efficiency with a relatively high indel rate. This is because of the low efficiency of coinfecting three
91 different viruses in the same cell (**Fig. 1a, Supplementary Fig. 1a**).

92 Packaging all PE3 components within the same virus is challenging. To increase PE
93 efficiency and facilitate a pooled screening approach with a lentiviral library, we infected MCF7
94 cells with lentivirus containing an nCas9 and M-MLV reverse transcriptase stable expression
95 cassette (**Fig. 1b**). After puromycin selection, we isolated multiple clones and selected one with
96 the highest nCas9 expression (**Fig. 1c**, RT-qPCR, clone #4, **Supplementary Fig. 1b**) for
97 subsequent experiments. The stable expression of nCas9/M-MLV allows for high efficiency
98 pegRNA/ngRNA packaging and lentiviral delivery, with greater editing efficiency than the co-
99 infection method (**Fig. 1d**). To further improve PE efficiency, we assessed editing efficiency using
100 three different structured RNA motifs (EvopreQ1, MLV-PK1, and MLV-PK2) at the 3' terminus of
101 the pegRNA⁷⁻⁹. Cells treated with pegRNAs containing scaffold structure RNA motifs exhibited
102 consistently higher editing efficiencies at both the *EMX1* and *FANCF* locus compared to using PE
103 without structured RNA motifs (**Supplementary Fig. 1c**), so we added evopreQ1 to the pegRNA

104 design for all pooled screens. Scaffold 1⁵ and 2¹⁰ had no significant effects on PE efficiency,
105 suggesting the feasibility of dual pegRNA and ngRNA delivery from the same viral particle (**Fig.**
106 **1d**). All PE experiments in clonal MCF7 cells (MCF7-nCas9/RT) exhibited relatively low indel rates
107 (0.7% to 1.95%). Thus, we used MCF7-nCas9/RT cells and lentiviral delivery of both the pegRNA
108 with scaffold 1 and ngRNA with scaffold 2 in the same construct (**Fig 1e**).



109
110 **Figure 1. Optimizing PE efficiency in mammalian cells using lentiviral delivery.**
111 (a) The different strategies tested for optimizing PE efficiency in MCF7 cell lines. Top: co-infecting
112 three different viruses to deliver PE machinery. Bottom: dual pegRNA/ngRNA viral infection of
113 clonal MCF7 line stably expressing nickase Cas9 (nCas9) and Moloney murine leukemia virus
114 reverse transcriptase (M-MLV RT). Two scaffolds and three different structured RNA motifs tested
115 are also shown. (b) Lentiviral construct for generating nCas9/RT expressing MCF7 clones. PuroR,
116 Puromycin resistance gene. M-MLV RT, Moloney murine leukemia virus reverse transcriptase.
117 (c) RT-qPCR analysis showing the relative expression of nCas9/RT in different clones, normalized
118 to the dCas9 expression of an established CRISPRi iPSC line (Yellow). Error bars represent the
119 s.e.m. (d) The editing efficiency and indel rate for *EMX1* and *FANCF* loci at 2 weeks and 4 weeks
120 after PE installation using two different RNA scaffolds. Error bars represent the s.d. (e) Improved
121 vector for expression of pegRNA and ngRNA for PRIME. RTT: reverse transcription template,
122 PBS: primer binding site.



123

124 **Supplementary Figure 1. Optimizing PE efficiency in MCF7 cell line.**

125 (a) Prime editing efficiency and indel rate by co-infection of pegRNA, ngRNA and nCas9/RT
126 expressing lentiviruses in MCF7 cells. (b) Immunofluorescent staining showing the localization of
127 nCas9/RT (red, FLAG tagged) in the nucleus (blue, DAPI) in MCF7-nCas9/RT cells. Scale bars,
128 1000 μ m. (c) Editing efficiency and indel rate by PE using three different structured RNA motifs
129 to the 3' terminus of pegRNAs at 2 and 4 weeks post infection in MCF7-nCas9/RT cells. Error
130 bars represent the s.d.

131

132 **PRIME enables nucleotide-resolution analyses of enhancer function**

133 Enhancers can modulate cell type-specific gene expression and are highly enriched with
134 disease-associated variants. Knowledge of the endogenous function for each nucleotide in
135 enhancers should reveal crucial transcription factors that govern enhancer activation and facilitate
136 the development of better models for gene regulatory networks and the prediction of disease-
137 associated non-coding variant regulatory effects. To test whether PRIME can quantify the impact
138 of each base in an enhancer, we focused on an MCF7-specific *MYC* enhancer identified from a
139 CRISPRi screen¹¹. This enhancer is located 405 kb downstream of *MYC* and displays enhancer
140 signatures, including open chromatin, H3K27ac, and H3K4me1 signals, in addition to forming a
141 chromatin loop with the *MYC* promoter (Fig. 2a). Deletion of this enhancer caused an 85%
142 downregulation of *MYC* expression in MCF7 cells confirming its enhancer activity for *MYC*

143 (**Supplementary Fig. 2a**). Since *MYC* downregulation is correlated with MCF7 cell survival¹², we
144 performed a PE-enabled high throughput saturation mutagenesis screen of this *MYC* enhancer
145 in MCF7 cells dependent on the cell survival phenotype (**Fig. 2b**).

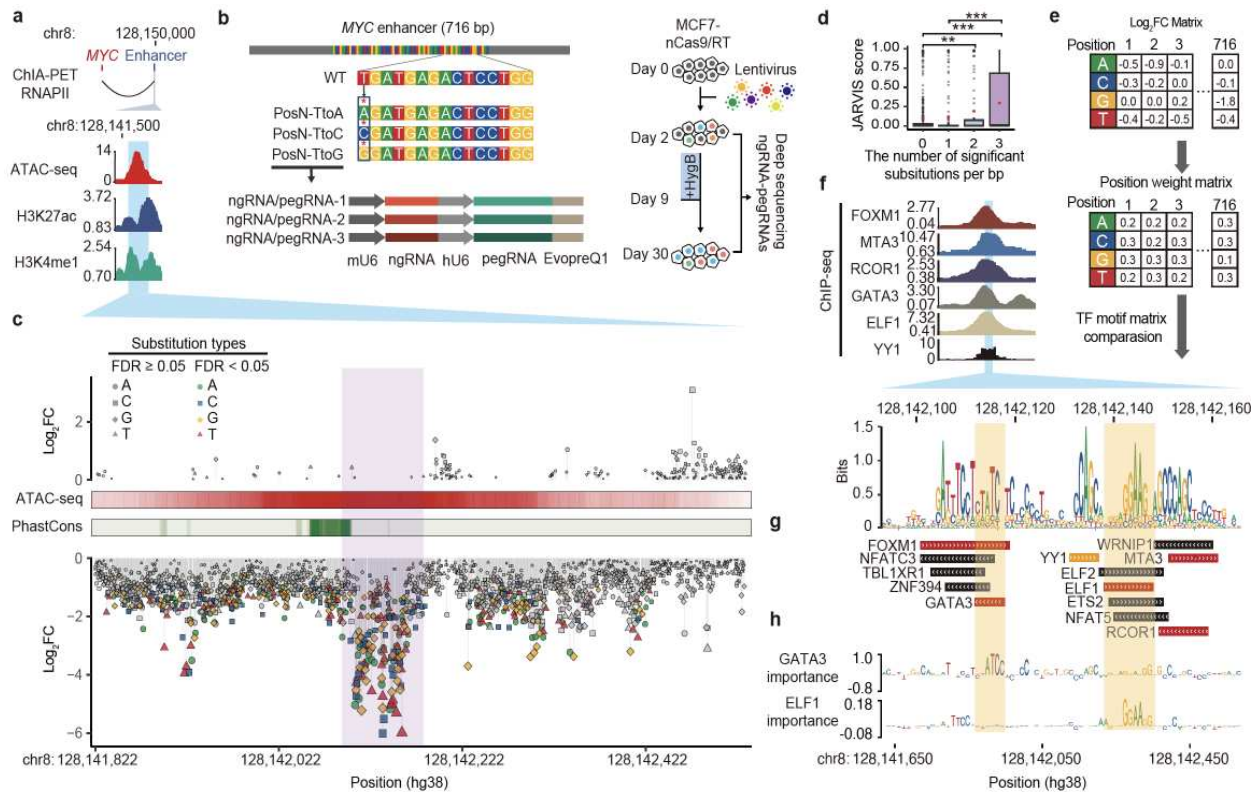
146 To dissect the enhancer's function at base-pair resolution, we designed a library of 6,252
147 pairs of pegRNA/ngRNA to generate 2,148 single nucleotide substitutions within the 716 bp *MYC*
148 enhancer region (**Supplementary Table 1**). Specifically, we changed the original base into three
149 other nucleotides, and each event was independently evaluated three times in the same screen
150 (**Fig. 2b**). We also included 94 positive control pegRNA/ngRNA pairs, which introduced stop
151 codons (iSTOPs) in *MYC*, and 400 negative control pegRNA/ngRNA pairs. 246 of the negative
152 controls were non-human genome targeting, and 154 targeted the AAVS1 safe harbor locus
153 (**Supplementary Table. 1**). We then infected MCF7-nCas9/RT cells with lentiviral libraries
154 expressing these pegRNA/ngRNA pairs (**Supplementary Fig. 2b**). Two days after infection,
155 virus-transduced cells were hygromycin selected for one week and expanded in regular media for
156 another 3 weeks. We collected cells at 2 and 30 days post-infection, amplified the integrated
157 pegRNA/ngRNA pairs, and determined the relative depletion or enrichment of each
158 pegRNA/ngRNA between these two time points by deep sequencing (**Fig. 2b**). We performed this
159 screen 3 times (**Supplementary Fig. 2c**) and used negative controls, including non-human
160 targeting and AAVS1 targeting paired pegRNA/ngRNAs for data normalization. Fold changes
161 (FC) for each pegRNA/ngRNA pair between day 2 and day 30 samples post-infection were
162 calculated using the MAGeCK pipeline¹³ (**Supplementary Table 1**). As expected, 78% (73/94) of
163 iSTOPs were depleted ($\log_2\text{FC} < 0$) 30 days post-infection. iSTOP depletion rates were negatively
164 correlated with their distance from the transcription start site (TSS) of *MYC*, consistent with the
165 observation that gene knockout is more efficient when perturbations are introduced at the 5'
166 terminus¹⁴ (**Supplementary Fig. 2d**). In addition, two iSTOPs (amino acid position 350 and 355)
167 targeting the region between the nuclear localization signal (NLS) and the carboxy-terminal
168 domain (CTD) domain were also significantly depleted (**Supplementary Fig. 2d**). The N-terminus
169 of *MYC* contains its core transcription transactivation domain which binds multiple partners¹⁵. It is
170 possible that those two iSTOPs created a truncated *MYC* still capable of binding to cofactors, but
171 unable to bind *MYC* DNA targets, interfering with the functions of wild type *MYC* and its cofactors.

172 To investigate the effects of each nucleotide on enhancer function, we defined sensitive
173 base pairs (SBP) as nucleotides that affect cell fitness when substituted at least once (FDR <
174 0.05, $|\log_2\text{FC}| > 1$). 334 of the 716 (46.6%) tested base pairs were SBP with $\log_2\text{FC} < -1$
175 (**Supplementary Table 1**), indicating that mutations at those locations reduce enhancer activity
176 and cell fitness. 23.1% (77/334) of SBPs were depleted at day 30 with all three substitutions (FDR

177 < 0.05, $\log_2\text{FC} < -1$). Additionally, none of the tested sequences were significantly enriched at day
178 30 with increased cell growth phenotype, indicating that perturbation of these sequences
179 exclusively attenuated enhancer activity (**Fig. 2c**).

180 Deep learning models have been developed to prioritize non-coding regions and predict
181 their relevance to human disease. Encouragingly, SBPs with two or more significant substitutions
182 ($n = 172$) were predicted to be more deleterious than SBPs with only one significant substitution
183 ($n = 162$) or non-SBPs ($n = 382$) by JARVIS¹⁶ (**Fig. 2d**). This demonstrates the success of PRIME
184 in validating computationally predicted functional sequences. We further established a continuous
185 bin density analysis, detecting variation in SBP density along the enhancer to define SBP-
186 enriched regions (**Supplementary Fig. 2e and f**). We identified the core enhancer region in the
187 enhancer with a high density of SBPs, based on the slope value of the cumulative curve of SBPs
188 with three significant substitutions, as a larger slope value indicates a higher density of SBPs in
189 the region. The core enhancer region was defined by a minimal slope cut-off of 0.43 (Z score-
190 derived $P < 0.05$). The core enhancer region (chr8:128,142,093-128,142,181, hg38) colocalized
191 with an open chromatin summit. This region contains SBPs with the most extensive fold changes
192 when mutated, indicating its strong effect on enhancer activity. (**Fig. 2c**, highlighted in purple).
193 Notably, the enhancer's core sequence was located next to a highly conserved region (**Fig. 2c**).
194 This is not surprising because enhancers undergo rapid evolutionary changes compared to
195 protein-coding sequences¹⁷.

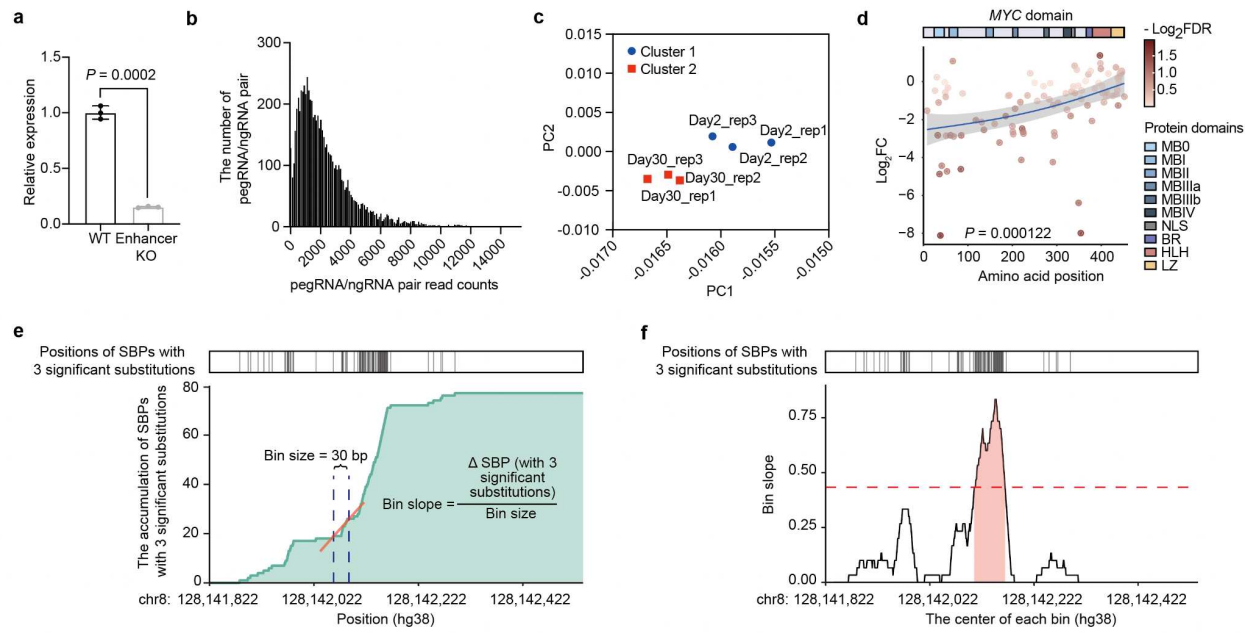
196 Our functional data provide a unique opportunity to calculate and construct a position
197 weight matrix (PWM). Using fold changes for each nucleotide, we generated a functional PWM
198 (**Fig. 2e**). Comparing our functional PWM with curated transcription factors (TFs) motifs from the
199 JASPAR, HOCOMOCO, and SwissRegulon databases¹⁸⁻²⁰ identified 13 TFs with matched motif
200 PWMs (**Fig. 2g and h, Supplementary Table 2**). 5 predicted TFs (GATA3, ELF1, FOXM1, MTA3
201 and RCOR1) have already been shown to bind to the *MYC* enhancer based on ENCODE ChIP-
202 seq datasets²¹, and YY1 is predicted to bind to this enhancer in MCF7 by Avocado through the
203 ENCODE project²² (**Fig. 2f**). Furthermore, GATA3 and YY1 are essential cell survival genes in
204 MCF7²³, confirming the utility of PE-enabled saturation mutagenesis for interrogating enhancer
205 function at base pair resolution. Essential nucleotides for the ELF1 and GATA3 binding motifs
206 identified by our screens were consistent with those imputed by BPNet²⁴, further validating the
207 importance of quantitative roles of each nucleotide discovered by PRIME. Combined, we
208 demonstrated that PRIME is useful for elucidating nucleotide-resolution functional annotations of
209 non-coding cis-regulatory elements.



210

211 **Figure 2. Functional characterization of a *MYC* enhancer by saturation mutagenesis using**
212 **PRIME.**

213 (a) (Top) The target enhancer is downstream of *MYC*. (Bottom) The enhancer region is highly
214 enriched with ATAC-seq, H3K27ac, and H3K4me1 ChIP-seq signals. The blue area indicates the
215 region selected for PRIME. (b) (Top) Diagram showing the design of saturation mutagenesis
216 screening at the 716 bp enhancer. Each nucleotide was subjected to substitution with three
217 nucleotides by PE. (Middle) Each substitution event was covered by three uniquely designed
218 pegRNA/ngRNA pairs. (Bottom) The PRIME workflow. (c) Log₂(fold change) of each substitution
219 at each base pair ordered by their genomic locations. Mutations with a significant effect on cell
220 fitness are colored. ATAC-seq signals and conservation scores calculated by PhastCons are
221 shown. (d) JARVIS scores for base pairs with different numbers of significant substitutions. Box
222 plots indicate median, IQR, Q1 - 1.5 × IQR, and Q3 + 1.5 × IQR. Outliers are shown as gray dots.
223 Mean values are shown as red dots. *P* values were calculated using a two-tailed two-sample t-
224 test. (e) The creation of a functional PWM for identifying potential TF binding sites. (f) (Top) ChIP-
225 seq signals of 6 TFs in MCF7. The blue region indicates the core enhancer region. (Bottom) The
226 sequence logo plot for the core enhancer regions generated by the functional PWM from (e). (g)
227 Matched TF binding sites. (h) (Top) Dense tracks showing BPNet model-derived nucleotide
228 importance scores for GATA3 and ELF1 binding sites.



229

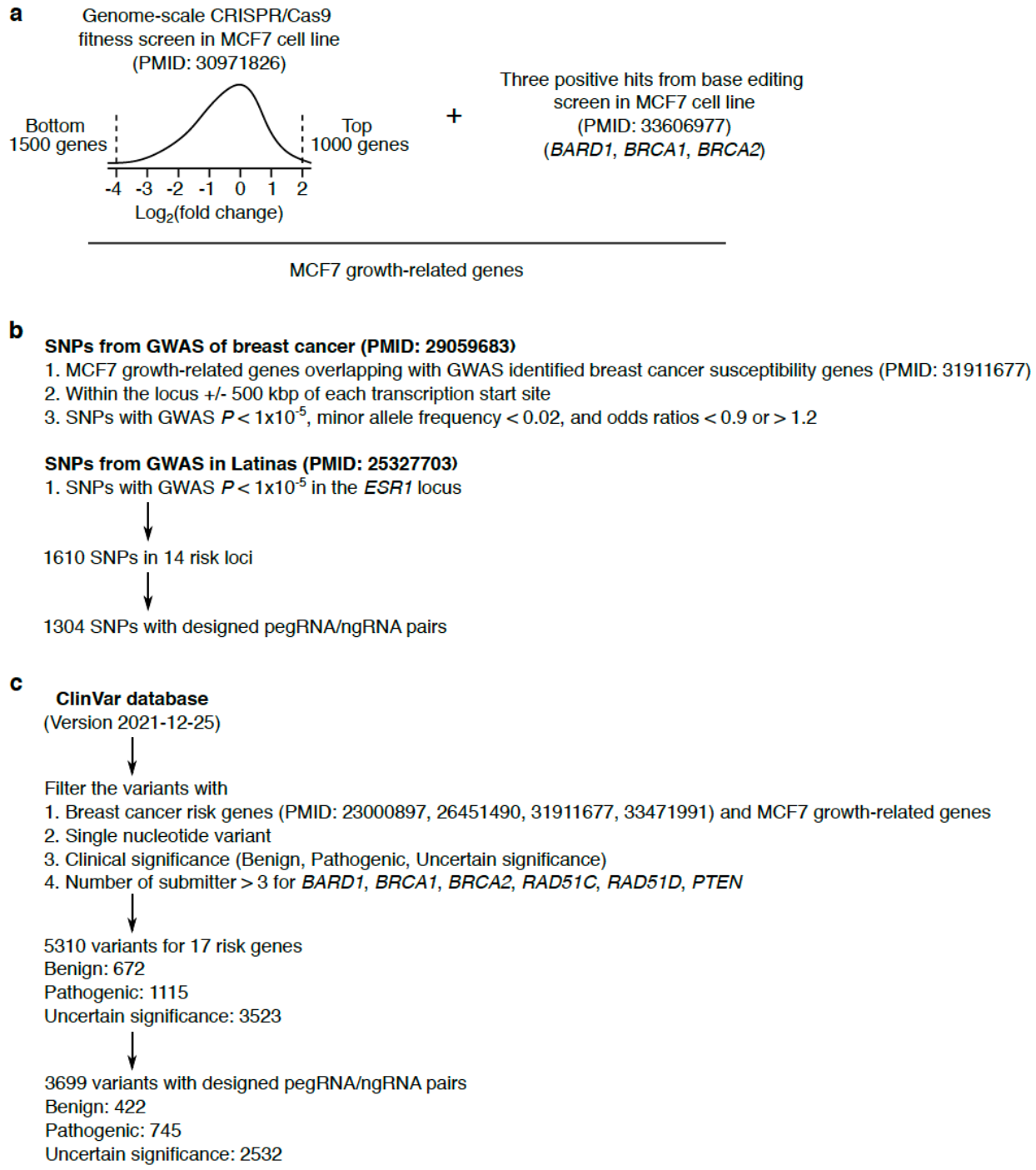
230 **Supplementary Figure 2. Characterize enhancer function and results of PRIME in MCF7**
 231 **cells.** (a) CRISPR/Cas9 knockout of the *MYC* enhancer in MCF7 decreased *MYC* expression. P
 232 values were calculated using a two-tailed two-sample t-test. Error bars represent the s.e.m. (b)
 233 Distribution of pegRNA/ngRNA pair read counts in the cloned plasmid library. (c) PCA analysis
 234 demonstrates the high reproducibility of PRIME between biological replicates. (d) The correlation
 235 between locations of PE-induced stop codons and their effect sizes. The blue line and P value
 236 were calculated using generalized additive models. The shaded areas indicate 95% confidence
 237 intervals. (e) (Top) The position of SBPs with three significant substitutions. (Bottom) Cumulative
 238 distribution plot of SBPs with three significant substitutions along the *MYC* enhancer and the
 239 formula for calculating the slope of each continuous bin. (f) Line plot of slopes for each continuous
 240 bin along the *MYC* enhancer. The red dashed line is the cutoff for a significant slope, which is
 241 based on a slope with a Z score-derived P value equal to 0.05. The red region is the core enhancer
 242 region, derived from the bins' slopes greater than the cutoff (slope > 0.43).

243

244 Characterization of breast cancer-associated variants

245 Next, we tested the feasibility of characterizing >5,000 disease-associated DNA variants
 246 at various genomic loci, including non-coding variants from GWAS and variants detected from
 247 clinical samples. For GWAS-identified variants, we focused on breast cancer, the most common
 248 cancer in women in the U.S. To test the feasibility of characterizing DNA variants associated with
 249 breast cancer, we used the summary statistics from the largest GWAS to date, including samples
 250 of mostly European ancestry²⁵. Candidate genes from a comprehensive fine mapping effort for

251 this GWAS²⁶ overlapping with growth phenotype genes prioritized by CRISPR screens^{23, 27} were
252 selected. These include: *CCND1*, *PSMD6*, *MYC*, *UBA52*, *DYNC1I2*, *ESR1*, *MRPS18C*, *NOL7*,
253 *EWSR1*, *BRCA2*, and *GRHL2*, which were negatively selected in a CRISPR knockout screen,
254 and *CUX1*, *CASP8*, and *TNFSF10*, which are tumor suppressor genes and positively selected in
255 a CRISPR knockout screen (**Supplementary Fig. 3a**). We then selected 1,304 single nucleotide
256 polymorphisms (SNPs) (**Supplementary Fig. 3b** and **Supplementary Table 3**) within 500 kbp
257 upstream and downstream of these genes that were previously associated with breast cancer²⁵
258 and had been implicated as possibly acting through these genes²⁶. We also selected 3,699
259 variants from the ClinVar database (**Supplementary Fig. 3c**), 2,840 of which were identified from
260 patients who were tested for hereditary breast cancer²⁸. To systematically assess variants' impact
261 on cell fitness, we designed two libraries: one to introduce reference alleles (Ref library) and
262 another to introduce alternative alleles (Alt library) targeting the selected variants (**Fig. 3a**)
263 (**Supplementary Table 3**). 250 non-targeting pegRNA/ngRNA pairs were added as negative
264 controls, respectively. For the Alt library, 115 pegRNA/ngRNA pairs introducing stop codons
265 (iSTOPs) in 23 MCF7 growth-related genes were included as positive controls, while
266 pegRNA/ngRNA pairs introducing reference sequences were used for those loci in the Ref library.
267 The cloned plasmids were packaged into lentiviral libraries and transduced into MCF7-nCas9/RT
268 cells. Cells were collected 2 and 32 days post infection, and pegRNA/ngRNA pairs were amplified
269 and deep sequenced (**Fig. 3b**). PRIME replicates using either Ref or Alt library (n = 4) were
270 reproducible at the read count level (**Supplementary Fig. 4a**).



271

272 **Supplementary Figure 3. Strategies for prioritizing genomic loci and clinical variants. (a)**
273 The MCF7 growth-related genes were selected from the CRISPR/Cas9 knockout screen and
274 base editing screen in MCF7 cells. (b) The strategy used for selecting breast cancer-related
275 SNPs. (c) The strategy used for selecting clinical variants.

276 From Alt library screens, 33.04% (38/115) of iSTOPs showed a significant cell fitness
277 effect (FDR < 0.05), which is comparable to the 31.8% positivity rate of iSTOPs for common
278 essential genes reported from the base editing screen in MCF7 cells²⁹. Furthermore, the fold
279 changes for iSTOPs were highly correlated with those for sgRNAs from MCF7 CRISPR knockout
280 screens of the same genes²³ (**Supplementary Fig. 4b**). More pegRNA/ngRNA pairs were
281 depleted (FDR < 0.05, Alt screen n = 322 and Ref screen n = 337) than enriched (FDR < 0.05,
282 Alt screen n = 148 and Ref screen n = 209) (binomial test, $P = 4.78 \times 10^{-8}$ for Alt screen and $P =$
283 6.85×10^{-16} for Ref screen) for both Alt and Ref screens on day 32 compared to day 2
284 (**Supplementary Fig. 4c and d, Supplementary Table 4, 5**). Theoretically, when a designed
285 peg/ngRNA pair matches the wild type MCF7 genotypes, they should have no effect on cell
286 growth. Notably, however, certain pegRNAs matching the wild type MCF7 genotype, exhibited
287 significant effects on cell growth beyond what was predicted, while the proportion of significant
288 hits for each genotype group were independent of initial MCF7 genotypes (Chi-square test $P =$
289 0.9998 on the Ref library and $P = 0.999$ on the Alt library, Cochran-Mantel-Haenszel test $P =$
290 0.9665 for the Ref library and Alt library together). For example, in the Ref library, 11.2% (59 out
291 of 528) of pegRNAs at sites with a Ref/Ref MCF7 genotype exhibited significant depletion, similar
292 to the 10.2% (55 out of 540) at heterozygous sites and 7.9% (18 out of 227) at Alt/Alt genotype
293 sites (**Fig. 3c**). These changes at sites where alleles were not expected to change suggests the
294 presence of undesired consequences of constitutive nCas9 expression, similar to CRISPR
295 inhibition (CRISPRi) once editing machinery is recruited to target sites³⁰. To test for potential
296 CRISPRi activity of nCas9 in PE, we compared the results between iSTOPs in the Alt library and
297 the corresponding pegRNA/ngRNA pairs in the Ref library. While pegRNAs in the Ref library
298 exhibited smaller effects on Day 32 compared to iSTOPs targeting the same loci, they were still
299 depleted on Day 32, confirming unintended consequences due to nCas9 occupancy at target
300 genomic loci (**Supplementary Fig. 4e**). Combined, we found that prolonged PE expression
301 exhibits undesired activity similar to CRISPRi, a crucial factor for consideration when analyzing
302 lentivirus-mediated PE screens.

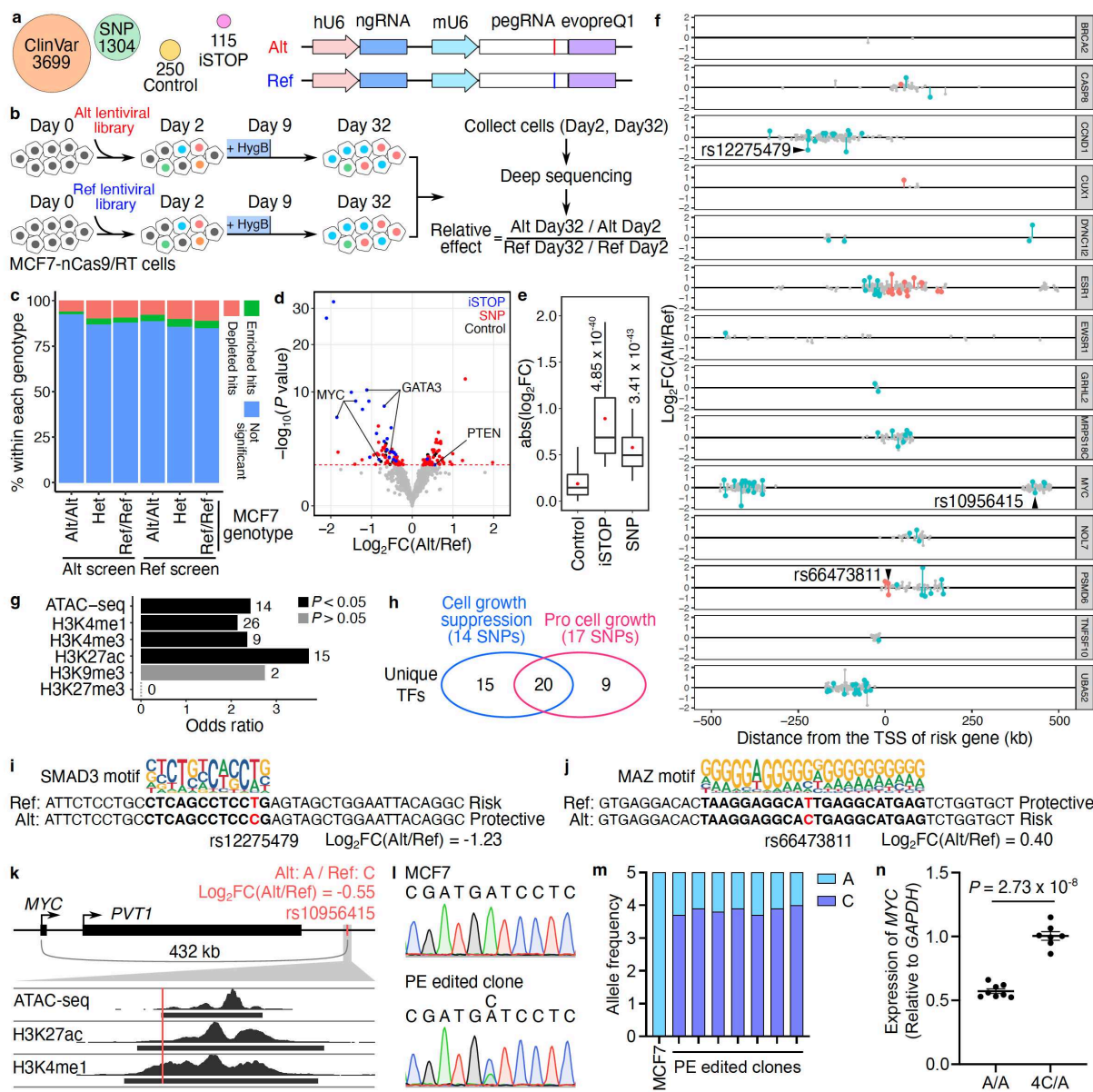
303 To correct for this undesired PE activity, we compared the ratio of FC for each
304 pegRNA/ngRNA pair from Alt and Ref screens by DESeq2³¹. We determined functional SNPs
305 based on their relative impact on cell growth between Alt and Ref PEs. In total, 56 SNPs with Ref
306 alleles and 47 SNPs with Alt alleles were identified to promote cell growth ($P < 0.05$, empirical
307 significance threshold to control type-I error at 5%, **Supplementary Fig. 4f, Fig. 3d**, and
308 **Supplementary Table 4**). As expected, identified functional SNPs had smaller effect sizes than
309 stop codons and significantly larger effect sizes than negative control PEs (**Fig. 3e**). Additionally,

310 iSTOPs for genes promoting cell growth, such as *MYC* and *GATA3*, were depleted, while the
311 iSTOP for the cell growth suppressor *PTEN* was enriched, validating our analysis approach (**Fig.**
312 **3d**).

313 Since risk variants can either be the Ref or Alt allele, we further annotated functional SNPs
314 based on genetic annotation of breast cancer risk variants. Since most GWAS SNPs are likely
315 not causal, we expected that only a fraction of the 1,304 tested SNPs would exhibit a biological
316 effect. We calculated the mean likelihood of a variant being causal using CAVIAR and found that
317 the mean expectation for a variant being causal was ~8.9% when we made the assumption of
318 only one causal variant in each linkage disequilibrium (LD) clump. If we allowed for more than
319 one causal variant in each LD clump the mean probability of being causal for the variants was
320 ~13.0%. Compared to the reference allele, 50 risk SNPs' alternative alleles were pro-growth, and
321 53 risk SNPs' alternative alleles reduced cell growth (**Fig. 3f**). 18.45% (19/103) of the functionally
322 validated risk SNPs were located within the risk gene's body. The rest were located in distal
323 regions with an average distance of 185.8 kb from the risk gene's TSS (**Fig. 3f**). All tested loci
324 contained at least one SNP with a significant effect on cell growth, except for the *BRCA2* locus,
325 in which only 2 SNPs were tested. Finally, identified functional SNPs were significantly enriched
326 for active chromatin marks (two-tailed Fisher's exact test, $P < 0.05$), including ATAC-seq,
327 H3K27ac, H3K4me1, and H3K4me3 signals, relative to their corresponding genomic background
328 (1 Mbp surrounding selected cell growth genes) (**Fig. 3g**).

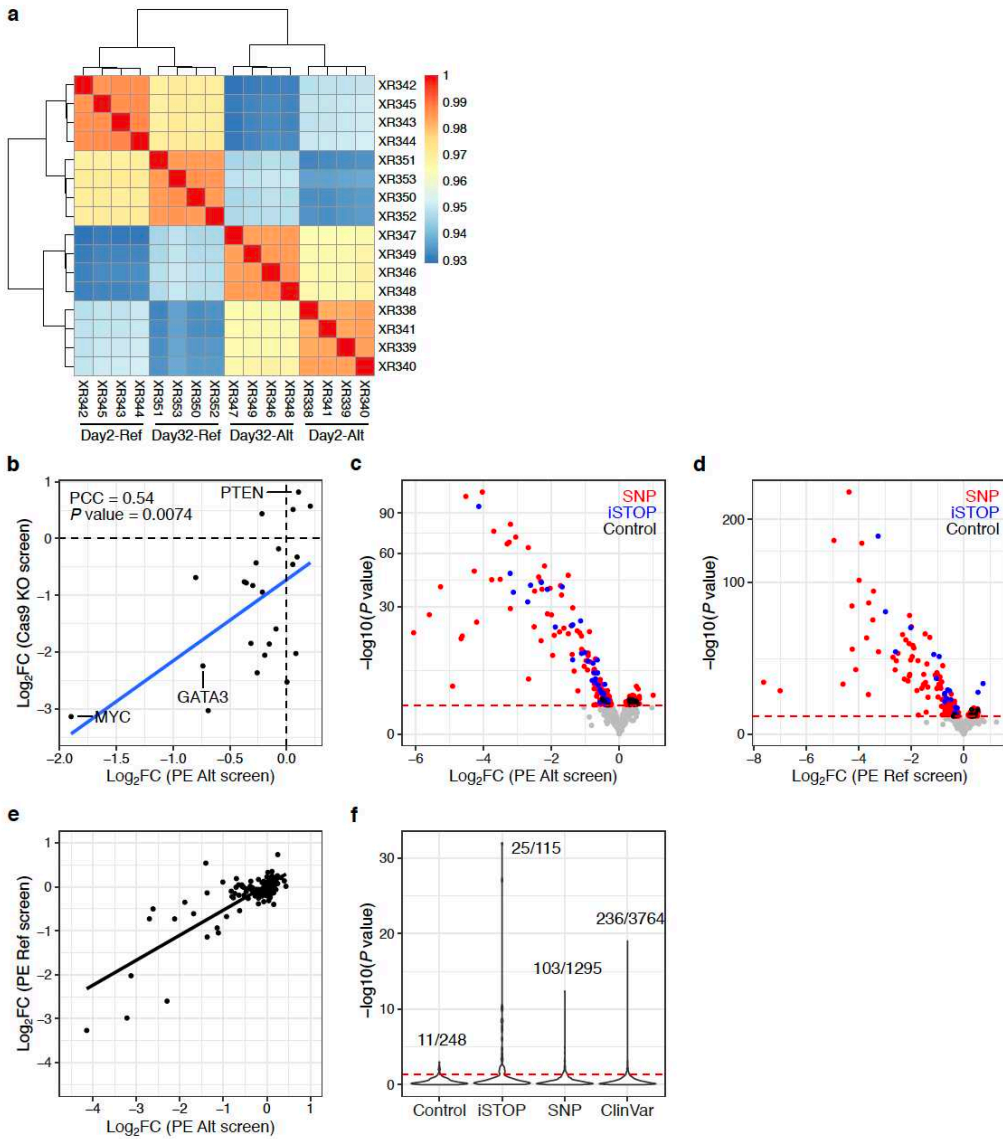
329 To explore potential mechanisms for functional SNPs' regulation of cell fitness changes,
330 we searched candidate TF binding motifs against the human motif database HOCOMOCO¹⁹ using
331 40 bp regions centered on 103 identified functional SNPs. We retrieved 281 and 391 motifs (FDR
332 < 0.05 and TF expression > 1 FPKM) containing Alt and Ref alleles, respectively. After removing
333 redundant motifs for each SNP locus, we identified 90 TF binding sites for 35 unique TFs
334 associated with the cell growth suppression phenotype ($\log_2\text{FC}(\text{Alt}/\text{Ref}) < 0$) and 55 sites for 29
335 unique TFs associated with the pro cell growth phenotype ($\log_2\text{FC}(\text{Alt}/\text{Ref}) > 0$) (**Fig. 3h** and
336 **Supplementary Table 6**). In particular, the Alt allele (protective allele), rs12275479 (T>C) at the
337 *CCND1* locus disrupts the SMAD3 binding motif and is associated with reduced cell growth in our
338 screens, consistent with the TGF β -SMAD3 axis decreased the number of mammosphere-
339 initiating cells in MCF7³² (**Fig. 3f and i**). In another example, we found that a MAZ binding site of
340 MAZ is affected by the rs66473811 (T>C) Alt allele at the *PSMD6* locus. MAZ is a transcription
341 factor that promotes breast cancer cell proliferation via driving tumor-specific expression of
342 *PPAR γ 1* gene and regulating *MYC* expression^{33, 34} in line with that Alt allele being the risk allele
343 (**Fig. 3f and j**). To validate our PRIME results, we selected rs10956415 from the *MYC* locus, which

344 exhibited a moderate effect on cell growth in the screen ($\text{Log}_2\text{FC}(\text{Alt}/\text{Ref}) = -0.55$) (Fig. 3f).
 345 rs10956415 is located in a candidate enhancer region 432 kb downstream of *MYC* (Fig. 3k).
 346 MCF7 cells are homozygous for the alternative allele (A) at the rs10956415 locus, which has a
 347 copy number of five in this cell line³⁵ (Fig. 3l and m). Using prime editing, we converted 4 copies
 348 of the alternative allele (A) to the reference allele (C) in seven independent clones, yielding a
 349 43.2% average increase in *MYC* expression compared to unedited cells with 5 copies of A alleles
 350 (Fig. 3m and n). Since *MYC* expression level positively correlates with MCF7 cell growth³⁶, the
 351 *MYC* expression of the PE edited clones is consistent with the cell growth phenotype of
 352 rs10956415 observed in the screening. Together, these results support the use of PRIME to
 353 functionally characterize GWAS-identified variants.



354

355 **Figure 3. PRIME reveals functional SNPs associated with breast cancer.** (a) Alt and Ref
356 library design overview. In the design, we included breast cancer-associated variants (SNP),
357 clinical variants (ClinVar), introduced stop codons (iSTOP), and non-targeting controls. For each
358 variant, pegRNA/ngRNA pairs introducing either the Alt or Ref allele were designed. (b) Workflow
359 of PRIME with Alt and Ref libraries. MCF7-nCas9/RT cells were infected with either lentiviral
360 library. Cells were collected on days 2 and 32 post-infection. The abundance of pegRNA/ngRNA
361 pairs in the samples collected on days 2 and 32 were deep sequenced. The relative effect of each
362 variant was determined based on its relative impact on cell growth between Alt versus Ref alleles.
363 (c) The percentage of significant hits (FDR < 0.05) identified from Alt and Ref screens for Alt/Alt,
364 Het, and Ref/Ref genotypes in MCF7. (d) The functional SNPs (red) with either a positive or a
365 negative impact on cell growth were determined by their relative effect in the Alt versus Ref
366 screens. Blue dots represent significant iSTOPs, and black dots represent controls. The red
367 dashed line indicates 0.05 FDR. (e) Absolute effects of identified functional iSTOPs and SNPs
368 are higher than the effects of negative controls (P values were calculated by two-tailed two-
369 sample t-test). (f) The genomic distance of SNPs tested at each risk locus relative to each gene's
370 TSS. Red dots are functional SNPs within gene bodies, blue dots are functional SNPs in distal
371 regions, and gray dots are SNPs with non-significant effects. (g) Relative enrichment of genomic
372 features for identified functional SNPs (P values were calculated by two-tailed Fisher's exact test).
373 The numbers of SNPs overlapping each genomic feature are labeled next to each bar. (h) Venn
374 diagram showing the numbers of unique transcription factors (TFs) with differential binding sites
375 centered on functional SNPs. The numbers of SNPs that alter TF binding sites are also in the
376 parentheses. (i, j) Examples of functional SNPs disrupting TF binding sites. (i) The Alt protective
377 allele of rs12275749 (position shown in f) affects the SMAD3 binding site and (j) The Alt risk allele
378 of rs66473811 (position shown in f) is matched with the MAZ binding motif. (k) rs10956415 located
379 within a candidate enhancer region overlapping with ATAC-seq, H3K27ac and H3K4me1 peaks
380 in MCF7 cells. (l) Representative Sanger sequencing results for the rs10956415 locus in unedited
381 MCF7 cells and a PE edited clone. (m) Allele frequencies of alternative (A) and reference (C)
382 alleles of rs10956415 in unedited MCF7 cells and PE edited clones. (n) Relative *MYC* expression
383 in control clones and PE edited clones ($P = 2.73 \times 10^{-8}$, two-tailed two-sample t-test).



384

385 **Supplementary Figure 4. Quality control and primary analysis of disease variants.** (a)
386 Heatmap with pairwise correlations and hierarchical clustering of read counts from PRIME. (b)
387 Pearson correlations between the \log_2 (fold change) of iSTOPs in the Alt library screen and the
388 \log_2 (fold change) of gRNAs in the CRISPR/Cas9 knockout screen for each target gene. (c)
389 Volcano plot of the results from the Alt library screen. (d) Volcano plot of the results from the Ref
390 library screen. (e) The \log_2 (fold change) for each iSTOP from the Alt and Ref library screens. (f)
391 Violin plot showing the 5% FDR cutoff used for the relative effect analysis comparing the Alt and
392 Ref libraries. Numbers above peaks indicate the significant data points versus the total data points
393 in each category when using 5% FDR. We used the 5% percentile of P values from negative
394 controls as the empirical significance threshold to achieve a false discovery rate (FDR) of 5%
395 indicated by the red dashed line in d-f.

396

397 **PRIME can characterize clinical variants of uncertain significance**

398 Genetic variants detected in clinical samples provide a valuable resource for
399 understanding the etiologies of human diseases. However, many clinically discovered variants
400 are annotated as Variants of Uncertain Significance (VUS) due to unpredictable functional
401 consequences, even in well-characterized protein-coding genes. To assess the capacity of
402 PRIME to functionally annotate VUS using MCF7 growth phenotypes, we designed
403 pegRNA/ngRNA pairs for 2,532 VUS, 745 pathogenic variants, and 422 benign variants for 17
404 genes (**Supplementary Fig. 3c** and **Supplementary Table 3**). 76.78% of the variants tested
405 were from breast cancer patients (**Supplementary Table 3**). By comparing the relative effect
406 sizes of each Alt and Ref allele pair, we identified 236 functional clinical variants affecting cell
407 growth in 15 genes, including 49 pathogenic variants, 156 VUS, and 31 benign variants (**Fig. 4a**
408 and **Supplementary Table 5**). The average effect sizes for pathogenic variants, VUS, and benign
409 variants were between that of negative controls and iSTOPs (**Fig. 4b**).

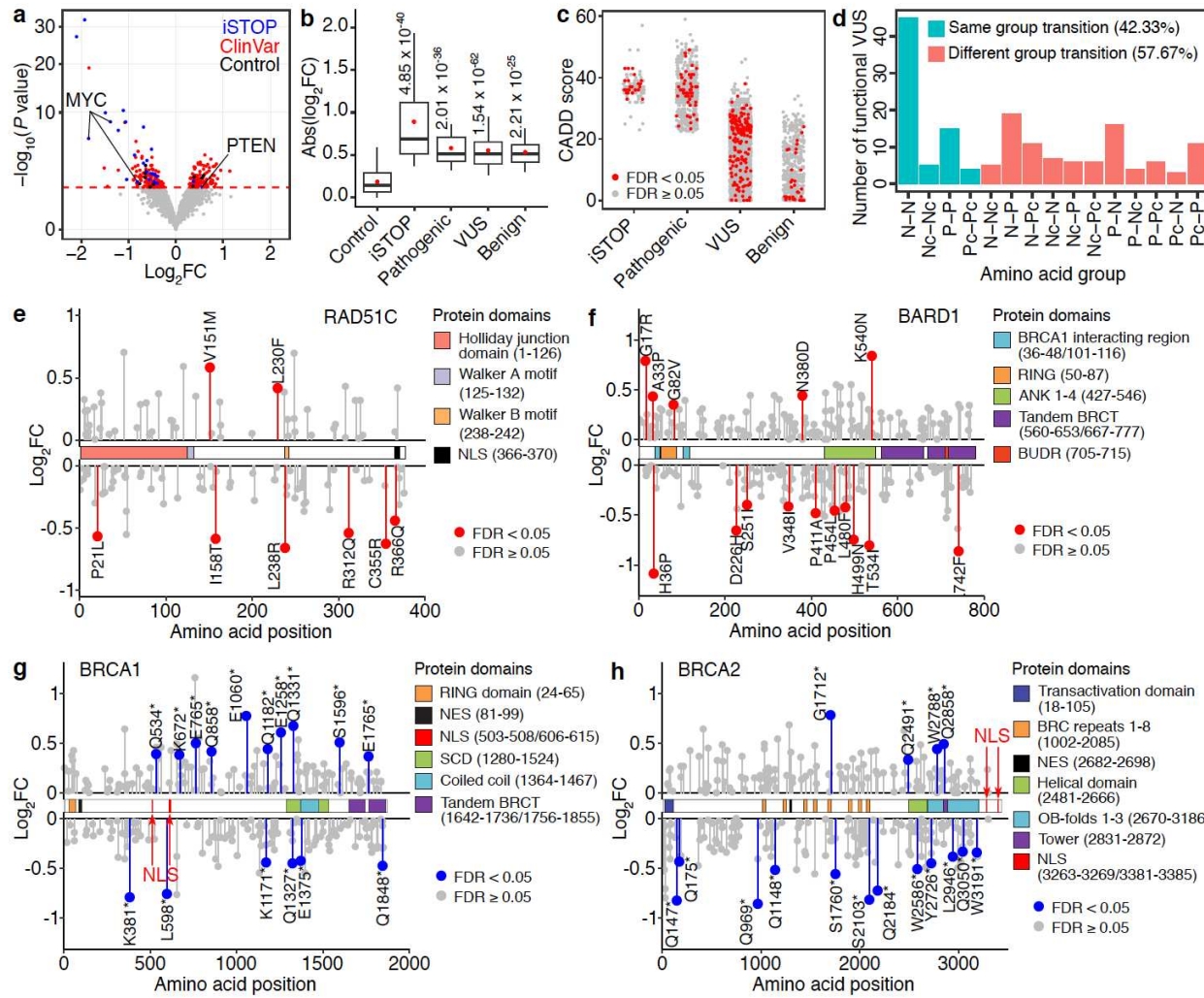
410 Several computational metrics have been used to assess the deleteriousness of variants³⁷,
411 ³⁸. One such method is CADD, which integrates diverse genome annotations into a single,
412 quantitative score estimating the relative pathogenicity of human genetic variants³⁷. iSTOPs and
413 pathogenic variants have similarly high CADD scores relative to other categories (**Fig. 4c**). The
414 CADD scores for the VUS and benign variants exhibit a broad distribution with median scores
415 much lower than those of iSTOPs and pathogenic variants. Interestingly, the CADD scores for
416 identified functional variants within the VUS or benign variant groups did not have higher CADD
417 scores as expected, indicating the limitation of solely relying on computational prediction for
418 variants annotation and underscoring the importance of validating clinical variants with functional
419 assays, even for those located in well-studied protein-coding genes. For example, one benign
420 variant in BARD1 (Arg378Ser) with a low CADD score (CADD = 4.317) would not be classified as
421 functional. However, this variant exhibited a significant cell growth suppression effect in MCF7
422 cells based on our screening results. BARD1 (Arg378Ser) can impair the nuclear localization of
423 the BRCA1/BARD1 complex, and synergistically promote tumor formation with BARD1
424 (Pro24Ser) *in vivo*³⁹. Furthermore, most of the identified functional VUS were missense variants,
425 and about half of the significant VUS from our screens changed amino acid type within the same
426 group based on polarity (**Fig 4d**), complicating the determination of their molecular
427 consequences. Our results offer novel insights into the potential roles of clinical variants in
428 disease pathogenesis through their modulation of cell fitness, and provide annotations for VUS
429 and benign variants previously uncharacterized.

430 Functional and structural domains are integral contributors to protein function. 60% of the
431 functional VUS identified are located within an annotated protein domain in the UniProt
432 database⁴⁰, supporting their pathogenicity. For example, we identified 8 VUS in *RAD51C* (**Fig.**
433 **4e**), a cancer susceptibility gene and an essential gene for MCF7 survival. Two variants, one
434 (Pro21Leu) in the *RAD51C* functional domain (amino acid: 1-126) for Holliday junction processing
435 and the other (Arg366Gln) in the NLS region (amino acid: 366-370), were associated with reduced
436 cell growth by our screens (**Fig. 4e**). We also identified functional variants that were not located
437 in any annotated domain, including a functional *RAD51C* VUS (Arg312Gln) associated with a
438 phenotype of reduced MCF7 growth (**Fig. 4e**). Since Arg312Trp in *RAD51C* results in homologous
439 recombination deficiency and reduced colony formation phenotypes in MCF10A cells, and
440 abolishes *RAD51C*-*RAD51D* interaction⁴¹, Arg312Gln may produce a similar pathogenic
441 consequence on protein function. When comparing the *RAD51C* sequence with other *RAD51*
442 family proteins, we observed functional VUS were located in both conserved and non-conserved
443 amino acids (**Supplementary Fig. 5a**), underscoring the challenge of predicting variant function
444 based solely on protein sequence conservation.

445 Protein-protein interaction (PPI) is another essential functional activity in many biological
446 processes. In this study, we also identified functional VUS located in protein binding regions with
447 the potential to affect PPI. For example, *BARD1* interacts with *BRCA1* through RING domains,
448 and *BRCA1*-*BARD1*'s ubiquitin ligase activity is indispensable for DNA double-strand break
449 repair^{42, 43}. We identified a functional VUS (His36Pro) in the *BARD1* RING domain (**Fig. 4f**),
450 suggesting the structural consequences of this clinical variant affecting *BARD1*-*BRCA1*
451 heterodimer formation (**Supplementary Fig. 5b**). Consistent with these findings, AlphaFold
452 predicts that the His36Pro variant disrupts hydrogen bond formation between His36 in *BARD1*
453 and Asp96 in *BRCA1* (**Supplementary Fig. 5c**).

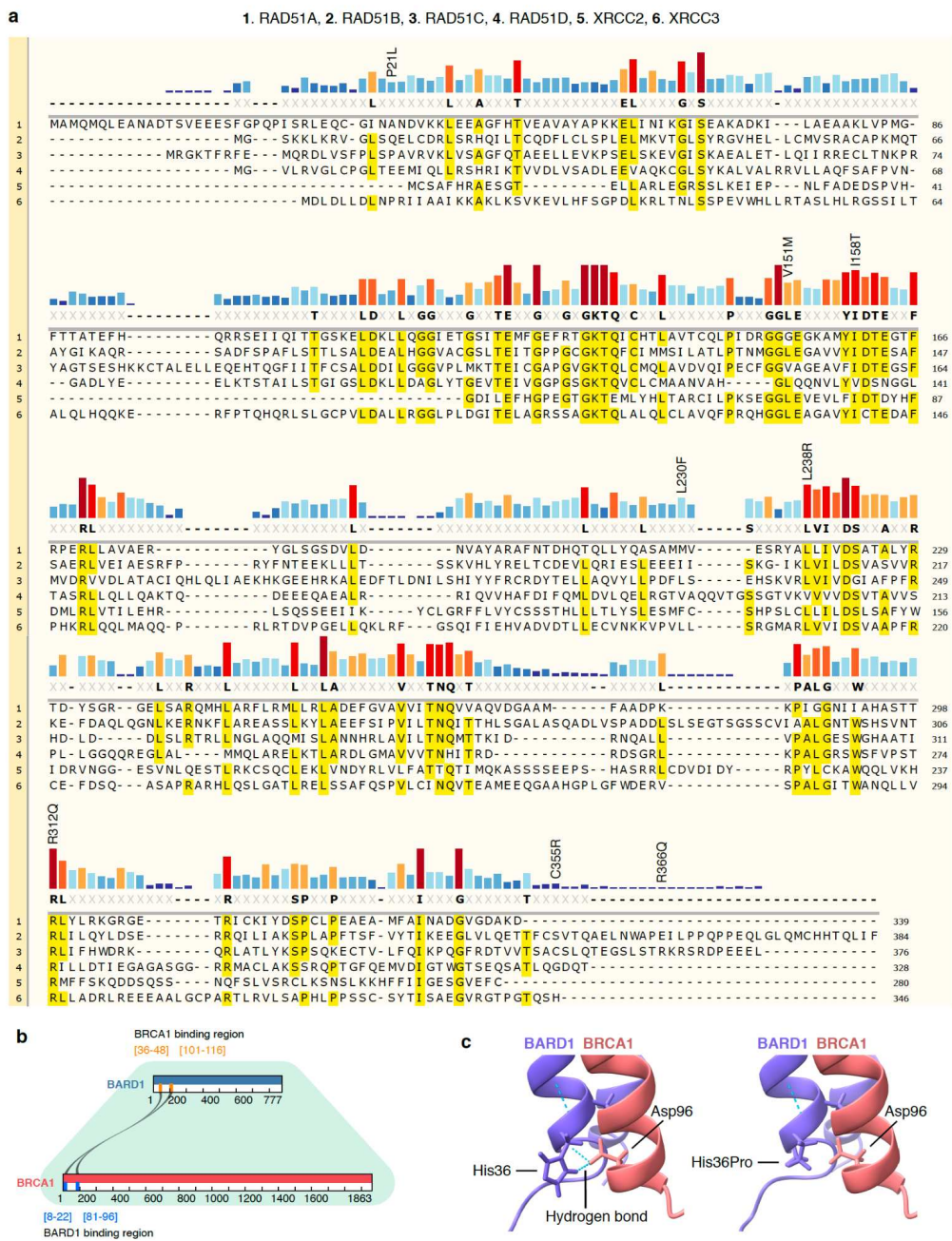
454 Nonsense mutations can generate new stop codons and truncated proteins. Although
455 most are annotated as pathogenic variants in ClinVar, the functional consequences of many
456 remain uncharacterized²⁸. In our screens, 563 nonsense clinical variants were tested in 13 breast
457 cancer risk genes with 38 variants identified as positive hits in 7 genes. Remarkably, 39.47%
458 (15/38) exhibited unexpected phenotypes compared to the knockout phenotypes of cell death of
459 these genes. Specifically, a similar number of functional nonsense variants in *BRCA1* (n = 15)
460 and *BRCA2* (n = 16) (**Fig. 4g, h**) were identified; however, 60% (9/15) in *BRCA1* could promote
461 MCF7 cell growth compared to 25% (4/16) in *BRCA2*. After locating variants within *BRCA1* and
462 *BRCA2*, we noticed that truncated proteins resulting from all gain-of-function nonsense variants
463 in *BRCA1* still retained their NLS. These results were confirmed by a different nonsense mutation

464 at Q858, located downstream of the NLS in BRCA1, which resulted in truncated BRCA1 with NLS
 465 and increased cell growth of MCF7²⁹. However, for all of the functional variants identified in
 466 BRCA2, their NLSs were located at the c-terminus⁴⁴ and were thus removed from the truncated
 467 proteins, leading to the loss of BRCA2 nuclear localization. Collectively, these results demonstrate
 468 the capability of PRIME to functionally characterize some nonsense mutations.



469
 470 **Fig 4. Functional clinical variants identified using PRIME.** (a) Functional clinical variants (red)
 471 with either a positive or a negative impact on cell growth were determined by relative effects on
 472 cell fitness between Alt and Ref alleles. Blue dots represent significant iSTOPs, and black dots
 473 represent negative controls. The red dashed line indicates 5% FDR. (b) Effect sizes of identified
 474 functional iSTOPs and clinical variants are larger than that of negative controls (P values were
 475 calculated by two-tailed two-sample t-test). Box plots indicate the median, IQR, $Q1 - 1.5 \times IQR$,
 476 and $Q3 + 1.5 \times IQR$. Red dots indicate the mean. (c) CADD scores for iSTOPs and clinical

477 variants. (d) Number of identified functional VUS causing each amino acid group transition. (N,
 478 Nonpolar; P, Polar; P_c, Positively charged; N_c, Negatively charged). (e,f) Lollipop plots of
 479 functional VUS in *RAD51C* and *BARD1* mapped to their canonical isoforms. The identified
 480 significant VUSs are labeled in red. Their effects on cell growth are indicated by fold changes.
 481 (g,h) Lollipop plots of the nonsense variants in *BRCA1* and *BRCA2* mapped to their canonical
 482 isoforms. The identified significant hits are labeled in blue. Their effects on cell growth are
 483 indicated by fold changes.



485 **Supplementary Figure 5. Examples of functional VUS with their potential consequences.**
486 (a) Sequence conservation of RAD51 family proteins. Alignment of RAD51 family proteins using
487 MUSCLE. Functional VUS identified by PRIME in RAD51C are labeled. (b) Graphic showing the
488 binding regions between BARD1 and BRCA1. (c) The Alphafold predicted protein structure of the
489 BARD1 and BRCA1 complex. Two hydrogen bonds were identified between wild type His36 in
490 BARD1 and Asp96 in BRCA1, but lost following the BARD1 His36Pro mutation.

491

492 **Discussion**

493 In this study, we describe a new genomic screening method, PRIME, to interrogate DNA
494 function at base-pair resolution by adopting and optimizing ‘search-and-replace’ prime editing^{5, 9}.
495 We demonstrate the success of pooled prime-editing screens to identify essential nucleotides in
496 a *MYC* enhancer via saturation mutagenesis screen, the functional characterization of 1,304
497 breast cancer-associated risk SNPs, and provide accurate annotation for 3,699 clinical variants.
498 Our study offers a novel strategy to elucidate genome function at an unprecedented precision and
499 scale. The broad applications demonstrated in this work suggest that PRIME can significantly
500 augment the functional characterization toolbox and advance our ability to elucidate the roles of
501 disease-associated variants in the human genome.

502 Our analyses show that lentiviral installation of PE yields long-lasting expression of nCas9,
503 pegRNA, and ngRNAs, but can result in unwanted sequence-specific repression similar to
504 CRISPRi. This bias must be corrected to produce accurate base-pair resolution annotations.
505 When assessing the functional impact of a variant, pegRNA controls should be included to
506 introduce other alleles at the same locus. Our study normalized sequence-specific repression
507 bias by comparing the differential effects on cell survival of all base pair substitutions at each
508 locus in the *MYC* enhancer, and between Alt and Ref alleles for disease variants. Additional
509 improvement could be achieved through controlled nCas9 expression duration. For example, a
510 doxycycline-inducible nCas9 could be selectively expressed when editing is needed and
511 reversibly turned off afterwards. In addition to establishing and optimizing PRIME, we defined
512 sensitive base pairs (SBPs) and core sequences for a *MYC* enhancer’s function. We generated
513 a functional PWM for this enhancer by leveraging effect sizes for all possible substitutions at each
514 base from the screens. The functional PWM enabled us to accurately predict TF binding sites
515 within the enhancer, providing critical annotations for delineating *MYC* activation in MCF7 cells.

516 Interpreting the effect of inherited genetic variations will dramatically advance our ability
517 to predict an individual’s disease risk. However, utilizing GWAS data for risk prediction is still
518 limited without substantial functional annotation. In this study, 7.9% of the 1,304 tested GWAS

519 breast cancer variants, and 6.2% of the 2,532 tested VUS were identified as significant hits with
520 functions linked to MCF7 growth phenotypes. Our results demonstrate the feasibility of PRIME
521 for functionally characterizing individual variants. The impact of variants was context-specific and
522 our findings were limited to assessing variants with growth phenotype related functions in MCF7
523 cells. Other ClinVar did not show changes in our functional assay likely have functional
524 consequences for breast cancer susceptibility genes in a different cell type or other biological
525 processes.

526 Future work employing different phenotypic screening readouts across multiple cell lines
527 will provide new insights into variant function. For example, screens that identify variants
528 associated with differential drug treatment responses will help construct better predictive models
529 for an individual's unique benefits and risks from therapeutics. Screens of variants with readouts
530 directly linked to physiological functions e.g. endolysosomal activities in microglia or synaptic
531 activities in neurons using iPSC models will uncover functional variants associated with
532 neuropsychiatric diseases. In summary, our study provides a roadmap to advance functional
533 genomics toward the actionable disease prediction, prevention and treatment necessary to realize
534 personalized medicine.

535

536 **Acknowledgements**

537 We thank Howard Y. Chang for sharing wild type MCF7 cells. This work was supported by the
538 Laboratory for Genomic Research Innovation Award LGRFU1019 and the George and Judy
539 Marcus Innovation Fund - Precision Medicine Innovation SBI2019 (to Y.S. and E.Z), the National
540 Institutes of Health (NIH) grants R01AG057497, R01EY027789, UM1HG009402, and
541 U01DA052713 (to Y.S.), U01HG011720 (to Y.L.). Sequencing was performed at the UCSF CAT,
542 supported by UCSF PBBR, RRP IMIA, and NIH 1S10OD028511-01 grants.

543

544 **Author contributions**

545 X.R. H.Y., and Y.S. conceived the study. Y.S. and E.Z. supervised the study. X.R. and H.Y.
546 designed PRIME screens. X.R. H.Y. C.B. Y.S. M.N. M.A.T. and V.N. performed experiments
547 under the supervision of Y.S. X.R. HY, J.L.N, Y.S. and J.C. performed computational analysis
548 under the supervision of Y.S. Y.L. and E.Z. Y.S. X.R. and H.Y. prepared the manuscript with
549 input from all other authors.

550

551 **Competing interests statement**

552 X.R., H.Y., and Y.S. have filed a patent application related to pooled prime editing screens.

553

554 **Code availability statement**

555 A copy of the custom code used for data analysis and figure generation in this study is available
556 upon request.

557

558 **Supplementary Tables**

559 **Supplementary Table 1. pegRNA and ngRNA oligo sequences and their fold changes in**
560 ***MYC* enhancer.**

561 **Supplementary Table 2. TF motif analysis for alleles based on functional data from PRIME.**

562 **Supplementary Table 3. pegRNA and ngRNA oligo sequences for SNP and ClinVar.**

563 **Supplementary Table 4. PRIME results for breast cancer-associated variants.**

564 **Supplementary Table 5. PRIME results for clinical variants.**

565 **Supplementary Table 6. TF motif analysis for alleles with functional SNPs for breast**
566 **cancer.**

567

568 **Methods**

569 **Cell culture**

570 MCF7 cells were cultured in Dulbecco's Modified Eagle Medium (DMEM) (Gibco, 10569010)
571 supplemented with 10% fetal bovine serum (FBS) (HyClone, SH30396.03), and were passaged
572 with trypsin-EDTA (Gibco, 25200072). All cells were cultured with 5% CO₂ at 37°C and verified to
573 be free of mycoplasma using the MycoAlert Mycoplasma Detection Kit (Lonza, LT07-218). Wild
574 type MCF7 cells were a gift from Howard Y. Chang's lab. The MCF7-nCas9/RT cell line was
575 generated by lentiviral transduction of cells with a cassette expressing the nickase Cas9 (nCas9)
576 Moloney murine leukemia virus reverse transcriptase (M-MLV RT) fusion protein. The infected
577 MCF7 cell pool was treated with puromycin (2.5 µg/ml) for two weeks. Then, single cells were
578 sorted into 96-well plates with one cell per well by fluorescence-activated cell sorting (FACS) to
579 generate a clonal MCF7-nCas9/RT cell line. nCas9/RT expression levels were quantified in each
580 clone via RT-qPCR, and normalized to the dCas9 expression level in a WTC11 doxycycline-
581 inducible dCas9-KRAB iPSC line^{45, 46}.

582

583 **Functional characterization of a *MYC* enhancer by CRISPR deletion**

584 Two sgRNAs were designed to knock out a MCF7 enhancer (chr8:128,141,747-128,142,627,
585 hg38) (sg1: GAAGTTGTAAGTATAGCGAG, sg2: AGTGCCTGGCACAGGCAGA). sgRNAs
586 were synthesized *in vitro* using the Precision gRNA Synthesis Kit (Invitrogen, A29377) according

587 to the manufacturer protocol and concentrations were quantified with Nanodrop. To deliver
588 genome editing machinery, 100 pmol of Cas9-NLS protein (QB3 MacroLab in University of
589 California, Berkeley) and 120 pmol of *in vitro* synthesized gRNA were electroporated into 250,000
590 MCF7 cells with the P3 primary nucleofection solution (Lonza, V4XP-3024), using the DN-100
591 Lonza 4D-Nucleofector program. Cells were then plated into 6-well plates and cultured for 2 days,
592 followed by plating into 96-well plates to pick single clones. Successful knockout clones were
593 identified by genomic PCR with the primers forward: CACCAGGACTTGAAGGCAGC and
594 reverse: CACTTCCCAACCTCAGTTCC. RT-qPCR was used to quantify *MYC* expression (*MYC*
595 forward primer: GTCCTCGGATTCTCTGCTCT, reverse primer
596 ATCTTCTTGTTCCTCCTCAGAGTC) and normalized to the *GAPDH* expression level (*GAPDH*
597 forward primer: ATTCCATGGCACCGTCAAGG, reverse primer
598 TTCTCCATGGTGGTGAAGACG).

599

600 **Cloning of prime editing plasmids**

601 To construct the lentiV2-EF1a-nCas9/RT plasmid, we first excised the U6-sgRNA cassette from
602 the lentiCRISPR v2 plasmid (Addgene, 52961) by dual KpnI and EcoRI digestion followed by
603 blunt end ligation. We further replaced the Cas9 cassette with an nCas9/M-MLV-RT cassette from
604 the pCMV-PE2 plasmid (Addgene, 132775). The lentiV2-pegRNA and lentiV2-ngRNA plasmids
605 were constructed by replacing the Cas9 and Puromycin sequences in the lentiCRISPR v2 plasmid
606 (Addgene, 52961), with hygromycin B and EGFP sequences. RNA motifs and sgRNA scaffolds
607 were further integrated by Gibson assembly.

608

609 **Testing prime editing efficiency**

610 To assess prime editing efficiencies at the *EMX1* and *FANCF* loci, we cloned paired
611 pegRNAs/ngRNAs into individual vectors. For lentivirus co-infection testing, we first infected
612 MCF7 cells with EF1a-nCas9/RT lentivirus followed by treatment with puromycin (2.5 µg/ml;
613 Sigma-Aldrich, P8833) for 2 weeks to eliminate uninfected cells. Then, EF1a-nCas9/RT-infected
614 cells were seeded in 24-well plates at 12,500 cells per well for pegRNA and ngRNA co-infection.
615 The infected cells were treated with hygromycin B (200 µg/ml; Gibco, 10687010) 48 hours after
616 infection, and were collected one week after infection for editing efficiency assessment. For
617 testing in the MCF7-nCas9/RT clonal line, we seeded cells in 24-well plates at 12,500 cells per
618 well, followed by lentiviral infection (pegRNA-mCherry and ngRNA-EGFP). Two days after
619 infection, mCherry and EGFP double-positive cells were isolated by FACS and cultured. Cultured
620 cells were then collected at 2 weeks and 4 weeks post-infection for editing efficiency assessment.

621 Genomic DNA was then extracted from each sample using the Wizard genomic DNA purification
622 kit (Promega, A1120). Genomic sites of interest were amplified from purified genomic DNA and
623 amplicons were sequenced on the Illumina NovaSeq 6000 platform. Briefly, sequencing libraries
624 were prepared using DNA primers amplifying target genomic loci of interest for the first round of
625 PCR (PCR1). Then, DNA primers containing index adapters were used for the second round of
626 PCR (PCR2) to add these adapters to PCR1 amplicons. Finally, dual indexing primers were used
627 for the third round PCR (PCR3) to add Illumina indexes to each PCR2 amplicon. Alignment of
628 amplicons to reference sequences was performed using CRISPResso2⁴⁷. For all prime editing
629 efficiency quantification, wild-type and edited amplicon frequencies were quantified using a 21 bp
630 window centered on either the 1 bp wild-type or edited sequence. The remaining amplicons were
631 classified as indels.

632

633 **SNP prioritization**

634 We selected 14 MCF7 growth-related genes overlapping with GWAS identified breast cancer
635 susceptibility genes²⁶. For each gene, we selected SNPs using the GWAS results from the Breast
636 Cancer Association Consortium²⁵. We identified genome-wide significant SNPs with GWAS $P <$
637 1×10^{-5} , minor allele frequency < 0.02 , and odds ratios < 0.9 or > 1.2 (representing approximately
638 the top and bottom quartiles of the odds ratio distribution for SNPs meeting the location, P value,
639 and MAF thresholds) for association with breast cancer within the locus ± 500 kb of each
640 transcription start site. We also separately selected SNPs with GWAS $P < 1 \times 10^{-5}$ in the *ESR1*
641 locus using GWAS results from a Latina population⁴⁸. We determined linkage disequilibrium (LD)
642 clumps among the selected SNPs using the LD Link R package⁴⁹ with an LD threshold of $R^2 >$
643 0.1. We then prioritized the most likely causal variants using CAVIAR⁵⁰, as those with a causal
644 posterior probability (> 0.1), the highest posterior probability (≤ 0.1), or most extreme odds ratio
645 in each haplotype block. We ran CAVIAR twice for each locus, once assuming only one causal
646 variant per LD clump, and again allowing for more than one causal variant in each LD clump.

647

648 **Clinical variant prioritization**

649 We retrieved clinical variants from the ClinVar database (accessed 2021-12-25), and all single
650 nucleotide variants (SNVs) were kept for the PRIME design (**Supplementary Fig. 3c**). We first
651 selected only the SNVs whose genes overlapped with breast cancer risk and MCF7 growth-
652 related genes. Next, we only retained SNVs in the benign, pathogenic and uncertain significance
653 categories. Further, for SNVs associated with *BARD1*, *BRCA1*, *BRCA2*, *RAD51C*, *RAD51D*, and
654 *PTEN*, we only retained the SNVs with more than three submitters, as there are thousands of

655 identified variants for these genes. Finally, our selection criteria yielded 5310 SNVs, of which we
656 successfully designed pegRNA/ngRNA pairs for 3699 SNVs.

657

658 **Design and construction of prime-editing libraries**

659 For nucleotide-resolution analyses of *MYC* enhancer function, paired pegRNAs/ngRNAs targeting
660 a 716 bp enhancer region were first designed using PrimeDesign's PooledDesign-Saturation
661 mutagenesis tool⁵¹. We optimized pegRNAs/ngRNAs pairs based on ngRNA pegRNA proximity
662 (more than 50 bp) and primer binding site (PBS) length (near 14 nt), redesigning the sequence
663 containing the BsmBI cutting sites (GAGACG, CGTCTC) or TTTTT. Next, we used GuideScan2
664 to assess the specificity and efficiency of each pegRNA and ngRNA spacer sequence. Spacer
665 sequences with low specificity were redesigned to improve the specificity. Finally, three different
666 pegRNA/ngRNA pairs were designed to target the same base pair for 93.0% (666/716) of the
667 substitutions. Each replicate pegRNA/ngRNA pair shared the same pegRNA and sgRNA spacer
668 sequences, and only the substitution alleles differed in the pegRNA extension sequence. To
669 design positive control guides, we used pegIT⁵² to generate pegRNA/ngRNA pairs which alter a
670 single base pair to introduce a stop codon within the *MYC* coding region. We selected the best
671 pegRNA/ngRNA pair for each position suggested by pegIT⁵². The *AAVS1* locus was selected as
672 the targeting pegRNA/ngRNA pair negative control region based on previous work⁵³, and guides
673 were designed as described above using PrimeDesign⁵¹. For non-targeting pegRNA/ngRNA
674 pairs, pegRNA and ngRNA spacer sequences and pegRNA extension sequences were selected
675 from the ENCODE non-targeting sgRNA reference data set
676 (<https://www.encodeproject.org/files/ENCFF058BPG/>). A guanine nucleotide was added to the 5'
677 end of all pegRNAs/ngRNAs with leading nucleotides other than G, to increase transcription
678 efficiency from the U6 promoter. We used the following template to link these component
679 sequences: 5'- CTTGGAGAAAAGCCTTGTGTT[ngRNA-spacer]GTTTAGAGACG[5nt-random-
680 sequence]CGTCTCACACC[pegRNA-
681 spacer]GTTTAGAGCTAGAAATAGCAAGTTAAAATAAGGCTAGTCCGTTATCAACTTGAAAA
682 AGTGGCACCGAGTCGGTGC[pegRNA extension]CCTAACACCGCGGGTTC-3'.

683

684 Library oligos for the *MYC* enhancer screen were synthesized by Twist Bioscience and amplified
685 using the NEBNext High-Fidelity 2× PCR Master Mix (NEB, M0541L), forward primer:
686 GTGTTTGAGACTATAATATCCCTTGGAGAAAAGCCTTGTGTT and reverse primer
687 CTAGTTGGTTAACGCGTAACTAGATAGAACCGCGGTGTTAGG. To amplify paired
688 PegRNA/ngRNA library oligos for enhancer saturation mutagenesis, we employed emulsion PCR

689 (ePCR) to reduce recombination of similar amplicons during PCR. Briefly, ninety-six 20 μ l ePCR
690 reactions were performed using 0.01 fmol of pooled oligos with NEBNext High-Fidelity 2 \times PCR
691 Master Mix (NEB, M0541S). Each 20 μ l PCR mix was combined with 40 μ l of oil-surfactant mixture
692 (containing 4.5 % Span 80 (v/v), 0.4 % Tween 80 (v/v) and 0.05 % Triton X-100 (v/v) in mineral
693 oil)⁵⁴. This mixture was vortexed at maximum speed for 5 min, briefly centrifuged, and placed into
694 the PCR machine for amplification. Thermocycler settings were: 98 °C for 30 s, then 26 cycles
695 (98 °C 10 s, 60 °C 20 s, 72 °C 30 s), then 72 °C for 5 min, and finally a 4 °C hold. The ramp rate
696 for each step was 2 °C/s. After PCR, individual reactions were combined and purified using the
697 QIAQuick PCR Purification Kit (Qiagen, 28104) following previously established guidelines⁵⁵.
698 Purified PCR products were then treated with Exonuclease I (NEB, M0568L) and purified using
699 1 \times AMPure XP beads (Beckman Coulter, A63881). The isolated ePCR products were then
700 inserted into a BsmBI-digested lentiV2-mU6-evopreQ1 vector via Gibson assembly (NEB,
701 E2621L). The assembled products were electroporated into Endura electrocompetent
702 Escherichia coli cells (Biosearch Technologies, 60242) and approximately 4,000 independent
703 bacterial colonies were cultured for each library. The resulting plasmid DNA was linearized by
704 BsmBI digestion, gel-purified, and ligated using T4 ligase (NEB, M0202M) to a DNA fragment
705 containing an sgRNA scaffold and the human U6 promoter. The resulting library was
706 electroporated into Endura electrocompetent Escherichia coli cells (Biosearch Technologies,
707 60242) and cultured as described above. The final plasmid library was extracted using the Qiagen
708 EndoFree Plasmid Mega Kit (Qiagen, 12381).

709
710 For the SNP and clinical variant screen Alt library, pegRNA/ngRNA pairs were designed using
711 PrimeDesign⁵¹. The sequences 200 bp upstream and downstream of each variant or iSTOP were
712 used as inputs for PrimeDesign. We generated initial pegRNA/ngRNA pairs using the following
713 parameters: number of pegRNAs per edit: 10, length of homology downstream: 10 nt, PBS length:
714 13 nt, maximum reverse transcription template (RTT) length: 50 nt, number of ngRNAs per
715 pegRNA: 10, ngRNA to pegRNA nicking distance: 50 and 75 bp. Next, a guanine nucleotide was
716 added to the 5' end of all pegRNAs/ngRNAs with leading nucleotides other than G to increase
717 transcription efficiency from the U6 promoter. pegRNA/ngRNA pairs containing BsmBI sites
718 (GAGACG, CGTCTC) or a TTTTT sequence in the pegRNA spacer, ngRNA spacer or pegRNA
719 extension were eliminated. pegRNA/ngRNA pairs were further selected to maximize specificity,
720 efficiency, and ngRNA to pegRNA distance while minimizing pegRNA to edit distance when
721 multiple pairs were available for the same locus. For non-targeting pegRNA/ngRNA pairs,
722 pegRNA spacer, ngRNA spacer and pegRNA extension sequences were selected from the

723 ENCODE non-targeting sgRNA reference data set
724 (<https://www.encodeproject.org/files/ENCFF058BPG/>). To design the Ref library, we used the
725 same pegRNA/ngRNA pairs as the Alt library, but replaced the alternative alleles in the pegRNA
726 extension sequences with the reference allele sequences. The final oligos adhered to the
727 following template architecture: 5'-CTTGTGGAAAGGACGAAACACC[ngRNA-
728 spacer]GTTTCGAGACG[6nt-random-sequence]CGTCTCTTGTGTT[pegRNA-
729 spacer]gttttagagctagaaaatagcaagttaaaataaggctagtccgttatcaactgaaaaagtggcaccgagtcgggtgc[pegR
730 NA extension]TTGACGCCGTTCTATCTAGTTAC-3'.

731

732 The Alt and Ref library oligos were synthesized by Twist Bioscience. The Alt and Ref plasmid
733 libraries were cloned separately using two-step cloning. First, the oligo pool for each library was
734 amplified with NEBNext High-Fidelity 2× PCR Master Mix (NEB, M0541L) and the following
735 primers: Forward primer: TCGATTCTTGGCTTATATATCTTGTGGAAAGGACGAAACAC,
736 Reverse primer: ATTTCTAGTTGGTTAACGCGTAACTAGATAGAACCGCGTCAA. PCR
737 products were purified via gel excision and column purification (Promega, A9282), followed by
738 insertion into the BsmBI-digested lentiV2-hU6-evopreQ1 vector by Gibson assembly (NEB,
739 E2621L). The assembled products were electroporated into Endura electrocompetent
740 Escherichia coli cells (Biosearch Technologies, 60242). About 25 million bacterial colonies were
741 cultured for each library, followed by purification with the QIAGEN Plasmid Maxi Kit (QIAGEN,
742 12163). For the second step, the resulting plasmid libraries from the first cloning step were
743 linearized by BsmBI digestion, gel-purified, and ligated using T4 ligase (NEB, M0202M) to a DNA
744 fragment containing an sgRNA scaffold and the mouse U6 promoter. The ligated products were
745 electroporated into Endura electrocompetent Escherichia coli cells (Biosearch Technologies,
746 60242), and about 40 million bacterial colonies were cultured for each library. The final plasmid
747 libraries were extracted with the Qiagen EndoFree Plasmid Mega Kit (Qiagen, 12381).

748

749 **Lentivirus production and titration**

750 To produce the lentiviral library, we used our previously described method⁴⁶. Briefly, 5 µg of
751 plasmid library, with 3 µg of psPAX (Addgene, 12260) and 1 µg of pMD2.G (Addgene, 12259)
752 packaging plasmids were cotransfected into 8 million HEK293T cells in a 10-cm dish
753 supplemented with 36 µl PolyJet (SigmaGen Laboratories, SL100688). The medium was replaced
754 12 hours after transfection and harvested every 24 hours thereafter for a total of three harvests.
755 Harvested viral media was filtered through a Millex-HV 0.45-µm polyvinylidene difluoride filter

756 (Millipore, SLHV033RS) and further concentrated via centrifugation using 100,000 NMWL
757 (nominal molecular weight limit) Ultra-15 centrifugal filter units (Amicon, UFC910008).

758

759 The lentiviral titer was determined by transducing 400,000 cells with increasing volumes (0, 1, 2,
760 5, 10, 20, and 40 μ l) of concentrated virus and polybrene (6 μ g/ml; Millipore, TR-1003-G). 48
761 hours after the transduction, cells were dissociated with Trypsin-EDTA (0.25%; Gibco, 25200056)
762 and seeded as two separate replicates; one treated with hygromycin B (200 μ g/ml; Gibco,
763 10687010) for four days, and another that was not. Finally, hygromycin-resistant and control cells
764 were counted to calculate the infected cell ratios and viral titers.

765

766 **Prime-editing screens**

767 We performed MYC enhancer screens in triplicate. We transfected MCF7-dCas9/RT cells with
768 lentivirus libraries at a multiplicity of infection (MOI) of 0.3 with a coverage of 1,000 transduced
769 cells per paired pegRNA/ngRNA. 48 hours later, approximately 10 million cells were harvested
770 as controls and the remaining cells were treated with hygromycin B (200 μ g/ml; Gibco, 10687010)
771 for 7 days. After antibiotic selection, the cells were maintained in DMEM supplemented with 10%
772 FBS for 30 days post infection, and 10 million cells were collected from the final cell population.

773

774 We performed Alt and Ref library screens in quadruplicate. We separately infected about 24
775 million MCF7-nCas9/RT cells with the lentivirus library for each replicate of the Alt and Ref
776 screens at an MOI of 0.5, with a cell coverage of 2,000 infected cells per pegRNA/ngRNA pair.
777 48 hours post infection, one-third of the infected cells were collected from each cell pool as control
778 samples (Day 2). The remaining cells were treated with hygromycin B (200 μ g/ml; Gibco,
779 10687010) for 7 days and cultured until 32 days post infection (Day 32).

780

781 **Generation of Illumina sequencing libraries**

782 Genomic DNA was extracted from each sample via cell lysis and digestion [100 mM tris-HCl (pH
783 8.5), 5 mM EDTA, 200 mM NaCl, 0.2% SDS, and proteinase K (100 μ g/ml)], phenol:chloroform
784 (Thermo Fisher Scientific, 17908) extraction, and isopropanol (Thermo Fisher Scientific,
785 BP2618500) precipitation. For the MYC enhancer screen, we applied ePCR during library
786 preparation to amplify the paired pegRNA/ngRNA sequences from each sample and reduce
787 recombination between similar sequences. Briefly, thirty 20 μ l ePCRs were performed using 400
788 ng of DNA for each reaction and NEBNext High-Fidelity 2 \times PCR Master Mix (NEB, M0541S) with
789 the following primers: Enh-lib-Forward:

790 TCCCTACACGACGCTTCCGATCTNNNNNCCTGGAGAAAAGCCTGTTT, Enh-lib-
791 Reverse: GGAGTTCAGACGTGTGCTTCCGATCTNNNNNGAACCGCGGTGTTAGG. ePCR
792 was performed as described previously to amplify pegRNA/ngRNA pairs from genomic DNA.
793 Thermocycler settings were 98 °C for 30 s, then 25 cycles (98 °C 10 s, 60 °C 20 s, 72 °C 1 min),
794 then 72 °C 5 min, and finally a 4 °C hold. The ramp rate for each step was 2°C/s. After PCR,
795 individual reactions were combined and purified using the QIAQuick PCR Purification Kit (Qiagen
796 28104) following previously established guidelines⁵⁵. Purified PCR products were then treated
797 with Exonuclease I (NEB, M0568L) and purified using 1× AMPure XP beads (Beckman Coulter,
798 A63881). Round one PCR amplicons were used in the 2nd round of PCR to add Illumina adapter
799 and index sequences. For the 2nd round PCR, we performed 6 ePCR reactions containing 0.023
800 ng of purified DNA each, using NEBNext High-Fidelity 2× PCR Master Mix (NEB, M0541S). The
801 2nd round PCR mixture was prepared and purified similarly to the 1st. Thermocycler settings were
802 98 °C for 30 s, then 12 cycles (98 °C 10 s, 60 °C 20 s, 72 °C 1 min), then 72 °C 5 min, and finally
803 a 4 °C hold. The ramp rate for each step was 2°C/s. For Alt and Ref screens, we amplified
804 pegRNA/ngRNA pair sequences from each sample using NEBNext High-Fidelity 2× PCR Master
805 Mix (NEB, M0541L) and the following primers: Alt-Ref-lib-Forward:
806 TCCCTACACGACGCTTCCGATCTNNNNCTTGAAAGGACGAAACACC, Alt-Ref-lib-
807 Reverse:
808 GGAGTTCAGACGTGTGCTTCCGATCTNNNNCGTAACTAGATAGAACCGCGTCAA.
809 Twenty-four 50 µl PCR reactions, each containing 600 ng genomic DNA, were performed for each
810 sample. Individual reactions were combined for each sample and column purified (Promega,
811 A9282). The purified products were then amplified by indexing PCR to add Illumina TruSeq
812 adaptors and sample index sequences with the following primers: Index-Forward:
813 aatgatacggcaccaccgagatctacac[8 bp index]acactcttccctacacgacgcttccgatct, Index-Reverse:
814 caagcagaagacggcatacgat[8 bp index]gtgactggagttcagacgtgtcttccgatct. The final libraries
815 were gel purified and sequenced with 150 bp paired-ends on the Illumina NovaSeq 6000 platform.
816

817 **Data processing and analysis of prime-editing data**

818 Sequencing libraries were first trimmed with 5 bp random sequences from read1 and read2, and
819 low quality reads were filtered out with the fastp tool before formal mapping. To calculate the read
820 counts, each pegRNA/ngRNA pair was included if it met the following criteria: (1) Read 1 exactly
821 matched the sequence containing a 20-21 nt ngRNA spacer and 5 bp flanking sequences; (2)
822 Read 2 exactly matched the reverse complementary sequence containing the full pegRNA
823 extension and 5 bp flanking sequences.

824

825 For PRIME of *MYC* enhancer, the MAGeCK (0.5.9) pipeline¹³ was used to estimate the statistical
826 significance and fold change for each pegRNA/ngRNA pair at the sgRNA level, and for each
827 substitution at the gene level in the cell population relative to controls. The non-targeting and
828 AAVS1 targeting pegRNAs were used as negative controls for normalization. To identify the core
829 enhancer region for the *MYC* enhancer based on the screening results, we first identified base
830 pairs with three significant substitutions (FDR < 0.05), and calculated the slopes for each
831 continuous bin (moving step = 1 bp, bin size = 30 bp, x axis: the position of each base pair, y axis:
832 the accumulation number of SBPs with three significant substitutions) (**Supplementary Fig. 2e**).
833 The slopes were then transformed into Z score-derived *P* values accordingly. The core enhancer
834 region was identified by merging overlapping significant bins (*P* value < 0.05).

835

836 For Alt and Ref library screens, oligos with zero reads for any sample were removed before the
837 following analysis. Oligo counts from all samples were passed into DESeq2 (1.38.0)³¹ and a
838 median-of-ratios method was used to normalize samples for varying sequencing depths.
839 Normalized read counts for each oligo were then modeled by DESeq2 as a negative binomial
840 distribution. We then used DESeq2 to check the fold changes for each oligo in Alt and Ref libraries
841 by comparing Day 32 to Day 2 data (design= ~ Replicate + Condition). We further estimated
842 relative effects between the reference and alternate alleles by adding an interaction term (design= ~
843 Replicate + Condition + Allele + Condition:Allele). Condition refers to the collection timepoint
844 (i.e. Day 32 or Day 2), and Allele refers to the allele category (i.e. Alt or Ref). Finally, a Wald test
845 was performed via DESeq2 to calculate the *P* value. To minimize false positive hits and achieve
846 an empirical FDR less than 5%, we then selected a *P* value cutoff corresponding to the fifth
847 percentile of *P* values from non-targeting control oligos.

848

849 Motif matrix comparison analysis

850 To identify potential transcription factor (TF) binding sites within the target *MYC* enhancer, we
851 established a new method based on motif comparison⁵⁶ to directly compare known TF motifs with
852 our base-pair resolution functional data. We first calculated the \log_2 (fold change) for each
853 substitution at each base pair with MAGeCK (0.5.9)¹³. The \log_2 (fold changes) of the wild type
854 alleles were set to 0. We then transformed the \log_2 (fold change) of each substitution into the
855 corresponding fold change value. We further constructed the position weight matrix by
856 normalizing the fold change of each allele per base pair to the sum of all unique alleles' fold
857 change per base pair. We further partitioned the enhancer sequence into multiple bins with

858 lengths of 5 and 10 base pairs. We only retained bins with an information content (IC) over 3 and
859 an 'N' content less than 10%. We then collected all TF motifs from JASPAR, HOCOMOCO, and
860 SwissRegulon databases with high expression in MCF7 cells (TPM > 10, GSE175204). Next, we
861 compared the filtered TF motif matrices with the enhancer bin matrix using Tomtom (P value <
862 0.05) to identify the potential TF binding sites at the enhancer. Finally, we only retained positive
863 TF motif hits overlapping at least 95% of the input sequences' essential base pairs (positions with
864 maximum probabilities > 0.5). Details about the best matching motifs are summarized in
865 **Supplementary Table 2**.

866

867 **Predicting base pair contribution to enhancer activity with BPNet**

868 We trained a convolutional neural network using BPNet consistent with the published approach²⁴
869 to explain the GATA3, ELF1, FOXM1, MTA3, and RCOR1 ChIP-seq data from ENCODE projects.
870 Briefly, the model inputs were 1kb sequences across each ChIP-seq peak locus, and
871 corresponding ChIP-seq control peaks were used as the bias track for training. The region from
872 chromosome 2 was used as the tuning set, and chromosomes 5, 6, 7, 10, and 14 were used as
873 the test set. The X and Y chromosomes were excluded. The remaining regions from other
874 chromosomes were used to train the model with default parameters. Once models were acquired
875 for each TF's ChIP-seq data, DeepLIFT was used to calculate each input sequence base pair's
876 contribution to enhancer activity. TF-MoDISco contribution scores were finally used to cluster and
877 determine consolidated TF motifs and map these to input peak regions.

878

879 **MCF7 genotyping analysis**

880 Sequence Read Archive (SRA) files for SRR7707725 and SRR7707726 (paired-end, two reads
881 per loci) were retrieved from BioProject PRJNA486532. We used bwa-mem v.0.7.17 to align
882 sequenced reads to the human reference genome hg38 for each run separately. The Picard tools,
883 SortSam, MarkDuplicates, AddOrReplaceReadGroups were then used to process the BAM files.
884 Finally, GATK v.4.2.5.0 was used to call SNPs and indels via local haplotype re-assembly
885 (HaplotypeCaller) followed by joint genotyping on a single-sample GVCF from HaplotypeCaller
886 (GenotypeGVCFs). Finally, CalcMatch v.1.1.2 was used to verify genotype consistency between
887 two runs.

888

889 **Motif scan and TF identification for alleles with functional breast cancer SNPs**

890 The sequences 20 bp upstream and downstream of each SNP (Alt and Ref alleles) were used as
891 input sequences for TF motif analysis. FIMO software (version 5.5.0)⁵⁷ was used to identify
892 matching motifs centered on the SNP regions against the human TF motif database HOCOMOCO

893 (v11 FULL)¹⁹. All FIMO motif scans were performed using default settings. Finally, TFs (FPKM
894 >1) with binding motifs overlapping target SNP loci were selected (FDR < 0.05, *P* value < 0.0001).
895

896 **Functional validation of rs10956415 using prime editing and RT-qPCR**

897 To validate the function of rs10956415 in MCF7 cells, we converted the alternative allele (A) to
898 the reference allele (C) at this locus using PE. To clone the ngRNA/pegRNA expression plasmid,
899 we amplified the fragment containing the ngRNA-mU6-pegRNA for the rs10956415 reference
900 allele (C) from the screening plasmid library, and inserted this fragment into the BsmBI-digested
901 lentiV2-hU6-evopreQ1 vector using Gibson assembly (NEB, E2621L). We verified the cloned
902 ngRNA/pegRNA plasmid sequence using Primordium whole-plasmid sequencing.

903

904 To perform PE, we transfected two million MCF7-dCas9/RT cells with 2000 ng of ngRNA/pegRNA
905 plasmid containing an EGFP marker using PolyJet (SignaGen Laboratories, SL100688). Five
906 days after transfection, we sorted the cells with the highest EGFP expression level (top 2%) into
907 96-well plates with 100 cells per well using FACS. Approximately two weeks later, we extracted
908 genomic DNA from half of the cells in each well and maintained the other half by seeding them in
909 a 24-well plate. We estimated the PE efficiency for each well by performing genotyping PCR
910 followed by Sanger sequencing. We then expanded the cells in the wells with the highest editing
911 efficiency to isolate clonal PE edited cell lines. We sorted the cell pool into 96-well plates with one
912 cell per well using FACS. Approximately two weeks later, we performed genotyping PCR followed
913 by Sanger sequencing to identify successfully edited clones. Deep sequencing was then
914 performed to quantify the copy number of edited alleles.

915

916 To assess the effect of rs10956415 on *MYC* expression, we used seven PE edited clones with
917 four copies of the C allele and one copy of the A allele. About two million cells from each sample
918 were used to extract total RNA with the RNeasy Plus Mini Kit (Qiagen, #74134), and 1 µg of RNA
919 was used to generate cDNA with the iScript cDNA Synthesis Kit (Bio-Rad, #1708890). We used
920 RT-qPCR to quantify *MYC* expression (forward primer: GTCCTCGGATTCTCTGCTCT, reverse
921 primer: ATCTTCTTGTTCCTCCTCAGAGTC), which was normalized to the *GAPDH* expression
922 level (forward primer: CCACTCCTCCACCTTGACG, reverse primer:
923 ATGAGGTCCACCACCCCTGTT).

924

925 **Protein structure prediction with AlphaFold**

926 To explore the impact of the BARD1 His36Pro mutation on BARD1/BRCA1 complex structure,
927 we predicted the wild type BARD1/BRCA1 and BARD1(His36Pro)/BRCA1 complex structures
928 with AlphaFold. We used the same amino acid chain which is used in the BARD1/BRCA1 complex
929 structure determined by NMR spectroscopy⁴² (BARD1, residues 26-122; BRCA1, residues 1-103)
930 as input for complex structure predictions. The amino acid chains of BARD1 and BRCA1 were
931 imported into the Google Colab Version of AlphaFold V2.2.4^{58, 59}, powered by Python 3 Google
932 Compute Engine. AlphaFold applied a multimer model in response to the duo-sequence
933 imputation, then searched the genetic database to determine the best suited multiple sequence
934 alignment (MSA) for the imported sequence and initiated structural prediction. To avoid
935 stereochemical violations, all structures are relaxed with AMBER model (Assisted Model Building
936 with Energy Refinement) using GPU acceleration. The resulting PDB files were imported into
937 UCSF Chimera X^{60, 61} for structure visualization. Protein chains were assigned different colors to
938 distinguish individual chains, and selected amino acid atomic structures and hydrogen bonds were
939 illustrated for interaction analysis. Finally, the real-time rendered complex structures were
940 exported using the snapshot function in Chimera X at the optimal visualization angle.

941

942 **References**

- 943 1. Taliun, D. et al. Sequencing of 53,831 diverse genomes from the NHLBI TOPMed
944 Program. *Nature* **590**, 290-299 (2021).
- 945 2. Shalem, O., Sanjana, N.E. & Zhang, F. High-throughput functional genomics using
946 CRISPR-Cas9. *Nat Rev Genet* **16**, 299-311 (2015).
- 947 3. Anzalone, A.V., Koblan, L.W. & Liu, D.R. Genome editing with CRISPR-Cas nucleases,
948 base editors, transposases and prime editors. *Nat Biotechnol* **38**, 824-844 (2020).
- 949 4. Chen, P.J. & Liu, D.R. Prime editing for precise and highly versatile genome manipulation.
950 *Nat Rev Genet* (2022).
- 951 5. Anzalone, A.V. et al. Search-and-replace genome editing without double-strand breaks or
952 donor DNA. *Nature* **576**, 149-157 (2019).
- 953 6. Erwood, S. et al. Saturation variant interpretation using CRISPR prime editing. *Nat*
954 *Biotechnol* **40**, 885-895 (2022).
- 955 7. Anzalone, A.V., Lin, A.J., Zairis, S., Rabadan, R. & Cornish, V.W. Reprogramming
956 eukaryotic translation with ligand-responsive synthetic RNA switches. *Nat Methods* **13**,
957 453-458 (2016).
- 958 8. Houck-Loomis, B. et al. An equilibrium-dependent retroviral mRNA switch regulates
959 translational recoding. *Nature* **480**, 561-564 (2011).
- 960 9. Nelson, J.W. et al. Engineered pegRNAs improve prime editing efficiency. *Nat Biotechnol*
961 **40**, 402-410 (2022).
- 962 10. Dang, Y. et al. Optimizing sgRNA structure to improve CRISPR-Cas9 knockout efficiency.
963 *Genome Biol* **16**, 280 (2015).
- 964 11. Chen, P.B. et al. Systematic discovery and functional dissection of enhancers needed for
965 cancer cell fitness and proliferation. *Cell Rep* **41**, 111630 (2022).
- 966 12. Cho, S.W. et al. Promoter of lncRNA Gene PVT1 Is a Tumor-Suppressor DNA Boundary
967 Element. *Cell* **173**, 1398-1412 e1322 (2018).
- 968 13. Li, W. et al. MAGeCK enables robust identification of essential genes from genome-scale
969 CRISPR/Cas9 knockout screens. *Genome Biol* **15**, 554 (2014).
- 970 14. Shalem, O. et al. Genome-scale CRISPR-Cas9 knockout screening in human cells.
971 *Science* **343**, 84-87 (2014).
- 972 15. Baluapuri, A., Wolf, E. & Eilers, M. Target gene-independent functions of MYC
973 oncoproteins. *Nat Rev Mol Cell Biol* **21**, 255-267 (2020).
- 974 16. Vitsios, D., Dhindsa, R.S., Middleton, L., Gussow, A.B. & Petrovski, S. Prioritizing non-
975 coding regions based on human genomic constraint and sequence context with deep
976 learning. *Nat Commun* **12**, 1504 (2021).
- 977 17. Villar, D. et al. Enhancer evolution across 20 mammalian species. *Cell* **160**, 554-566
978 (2015).
- 979 18. Fornes, O. et al. JASPAR 2020: update of the open-access database of transcription
980 factor binding profiles. *Nucleic Acids Res* **48**, D87-D92 (2020).
- 981 19. Kulakovskiy, I.V. et al. HOCOMOCO: towards a complete collection of transcription factor
982 binding models for human and mouse via large-scale ChIP-Seq analysis. *Nucleic Acids*
983 *Res* **46**, D252-D259 (2018).
- 984 20. Pachkov, M., Balwierz, P.J., Arnold, P., Ozonov, E. & van Nimwegen, E. SwissRegulon,
985 a database of genome-wide annotations of regulatory sites: recent updates. *Nucleic Acids*
986 *Res* **41**, D214-220 (2013).
- 987 21. Consortium, E.P. An integrated encyclopedia of DNA elements in the human genome.
988 *Nature* **489**, 57-74 (2012).
- 989 22. Schreiber, J., Durham, T., Bilmes, J. & Noble, W.S. Avocado: a multi-scale deep tensor
990 factorization method learns a latent representation of the human epigenome. *Genome Biol*
991 **21**, 81 (2020).

992 23. Behan, F.M. et al. Prioritization of cancer therapeutic targets using CRISPR-Cas9
993 screens. *Nature* **568**, 511-516 (2019).

994 24. Avsec, Z. et al. Base-resolution models of transcription-factor binding reveal soft motif
995 syntax. *Nat Genet* **53**, 354-366 (2021).

996 25. Michailidou, K. et al. Association analysis identifies 65 new breast cancer risk loci. *Nature*
997 **551**, 92-94 (2017).

998 26. Fachal, L. et al. Fine-mapping of 150 breast cancer risk regions identifies 191 likely target
999 genes. *Nat Genet* **52**, 56-73 (2020).

1000 27. Hanna, R.E. et al. Massively parallel assessment of human variants with base editor
1001 screens. *Cell* **184**, 1064-1080 e1020 (2021).

1002 28. Landrum, M.J. et al. ClinVar: improvements to accessing data. *Nucleic Acids Res* **48**,
1003 D835-D844 (2020).

1004 29. Cuella-Martin, R. et al. Functional interrogation of DNA damage response variants with
1005 base editing screens. *Cell* **184**, 1081-1097 e1019 (2021).

1006 30. Qi, L.S. et al. Repurposing CRISPR as an RNA-guided platform for sequence-specific
1007 control of gene expression. *Cell* **152**, 1173-1183 (2013).

1008 31. Love, M.I., Huber, W. & Anders, S. Moderated estimation of fold change and dispersion
1009 for RNA-seq data with DESeq2. *Genome Biol* **15**, 550 (2014).

1010 32. Bruna, A. et al. TGFbeta induces the formation of tumour-initiating cells in claudinlow
1011 breast cancer. *Nat Commun* **3**, 1055 (2012).

1012 33. Bossone, S.A., Asselin, C., Patel, A.J. & Marcu, K.B. MAZ, a zinc finger protein, binds to
1013 c-MYC and C2 gene sequences regulating transcriptional initiation and termination. *Proc
1014 Natl Acad Sci U S A* **89**, 7452-7456 (1992).

1015 34. Wang, X. et al. MAZ drives tumor-specific expression of PPAR gamma 1 in breast cancer
1016 cells. *Breast Cancer Res Treat* **111**, 103-111 (2008).

1017 35. Ghandi, M. et al. Next-generation characterization of the Cancer Cell Line Encyclopedia.
1018 *Nature* **569**, 503-508 (2019).

1019 36. Wang, Y.H. et al. Knockdown of c-Myc expression by RNAi inhibits MCF-7 breast tumor
1020 cells growth in vitro and in vivo. *Breast Cancer Res* **7**, R220-228 (2005).

1021 37. Kircher, M. et al. A general framework for estimating the relative pathogenicity of human
1022 genetic variants. *Nat Genet* **46**, 310-315 (2014).

1023 38. Pollard, K.S., Hubisz, M.J., Rosenbloom, K.R. & Siepel, A. Detection of nonneutral
1024 substitution rates on mammalian phylogenies. *Genome Res* **20**, 110-121 (2010).

1025 39. Li, W. et al. A synergistic effect of BARD1 mutations on tumorigenesis. *Nat Commun* **12**,
1026 1243 (2021).

1027 40. UniProt, C. UniProt: the universal protein knowledgebase in 2021. *Nucleic Acids Res* **49**,
1028 D480-D489 (2021).

1029 41. Prakash, R. et al. Homologous recombination-deficient mutation cluster in tumor
1030 suppressor RAD51C identified by comprehensive analysis of cancer variants. *Proc Natl
1031 Acad Sci U S A* **119**, e2202727119 (2022).

1032 42. Brzovic, P.S., Rajagopal, P., Hoyt, D.W., King, M.C. & Klevit, R.E. Structure of a BRCA1-
1033 BARD1 heterodimeric RING-RING complex. *Nat Struct Biol* **8**, 833-837 (2001).

1034 43. Densham, R.M. et al. Human BRCA1-BARD1 ubiquitin ligase activity counteracts
1035 chromatin barriers to DNA resection. *Nat Struct Mol Biol* **23**, 647-655 (2016).

1036 44. Spain, B.H., Larson, C.J., Shihabuddin, L.S., Gage, F.H. & Verma, I.M. Truncated BRCA2
1037 is cytoplasmic: implications for cancer-linked mutations. *Proc Natl Acad Sci U S A* **96**,
1038 13920-13925 (1999).

1039 45. Mandegar, M.A. et al. CRISPR Interference Efficiently Induces Specific and Reversible
1040 Gene Silencing in Human iPSCs. *Cell Stem Cell* **18**, 541-553 (2016).

1041 46. Ren, X. et al. Parallel characterization of cis-regulatory elements for multiple genes using
1042 CRISPRpath. *Sci Adv* **7**, eabi4360 (2021).

1043 47. Clement, K. et al. CRISPResso2 provides accurate and rapid genome editing sequence
1044 analysis. *Nat Biotechnol* **37**, 224-226 (2019).

1045 48. Fejerman, L. et al. Genome-wide association study of breast cancer in Latinas identifies
1046 novel protective variants on 6q25. *Nat Commun* **5**, 5260 (2014).

1047 49. Machiela, M.J. & Chanock, S.J. LDlink: a web-based application for exploring population-
1048 specific haplotype structure and linking correlated alleles of possible functional variants.
1049 *Bioinformatics* **31**, 3555-3557 (2015).

1050 50. Hormozdiari, F., Kostem, E., Kang, E.Y., Pasaniuc, B. & Eskin, E. Identifying causal
1051 variants at loci with multiple signals of association. *Genetics* **198**, 497-508 (2014).

1052 51. Hsu, J.Y. et al. PrimeDesign software for rapid and simplified design of prime editing guide
1053 RNAs. *Nat Commun* **12**, 1034 (2021).

1054 52. Anderson, M.V., Haldrup, J., Thomsen, E.A., Wolff, J.H. & Mikkelsen, J.G. pegIT - a web-
1055 based design tool for prime editing. *Nucleic Acids Res* **49**, W505-W509 (2021).

1056 53. Chen, C.H. et al. Improved design and analysis of CRISPR knockout screens.
1057 *Bioinformatics* **34**, 4095-4101 (2018).

1058 54. Williams, R. et al. Amplification of complex gene libraries by emulsion PCR. *Nat Methods*
1059 **3**, 545-550 (2006).

1060 55. Verma, V., Gupta, A. & Chaudhary, V.K. Emulsion PCR made easy. *Biotechniques* **69**,
1061 421-426 (2020).

1062 56. Gupta, S., Stamatoyannopoulos, J.A., Bailey, T.L. & Noble, W.S. Quantifying similarity
1063 between motifs. *Genome Biol* **8**, R24 (2007).

1064 57. Grant, C.E., Bailey, T.L. & Noble, W.S. FIMO: scanning for occurrences of a given motif.
1065 *Bioinformatics* **27**, 1017-1018 (2011).

1066 58. Jumper, J. et al. Highly accurate protein structure prediction with AlphaFold. *Nature* **596**,
1067 583-589 (2021).

1068 59. Mirdita, M. et al. ColabFold: making protein folding accessible to all. *Nat Methods* **19**, 679-
1069 682 (2022).

1070 60. Goddard, T.D. et al. UCSF ChimeraX: Meeting modern challenges in visualization and
1071 analysis. *Protein Sci* **27**, 14-25 (2018).

1072 61. Pettersen, E.F. et al. UCSF ChimeraX: Structure visualization for researchers, educators,
1073 and developers. *Protein Sci* **30**, 70-82 (2021).

1074